

Radio-continuum detections of Galactic Planetary Nebulae

I. MASH PNe detected in large-scale radio surveys.

I. S. Bojčić,¹ Q. A. Parker,^{1,2} M. D. Filipović,³ D. J. Frew¹

¹*Department of Physics and Astronomy, Macquarie University, Sydney, NSW 2109, Australia*

²*Australian Astronomical Observatory, Epping, NSW 1710, Australia*

³*University of Western Sydney, Locked Bag 1797, Penrith South DC, NSW 1797, Australia*

Accepted ... Received ...; in original form ...

ABSTRACT

We present an updated and newly compiled radio-continuum data-base for MASH PNe detected in the extant large scale “blind” radio-continuum surveys (NVSS, SUMSS/MGPS-2 and PMN) and, for a small number of MASH PNe, observed and detected in targeted radio-continuum observations. We found radio counterparts for approximately 250 MASH PNe. In comparison with the percentage of previously known Galactic PNe detected in the NVSS and MGPS-2 radio-continuum surveys and according to their position on the flux density-angular diameter and the radio brightness temperature evolutionary diagrams we conclude, unsurprisingly, that the MASH sample presents the radio-faint end of the known Galactic PNe population. Also, we present radio-continuum spectral properties of a small sub-sample of MASH PNe located in the strip between declinations -30° and -40° , that are detected in both the NVSS and MGPS-2 radio surveys.

Key words: astronomical data bases: miscellaneous - planetary nebulae: general - radiation mechanisms: thermal - radio continuum: ISM

1 INTRODUCTION

Planetary nebulae (PNe) are ionized, gaseous envelopes ejected from intermediate-mass stars ($1-8 M_\odot$) in the final stage of their evolution. At radio frequencies the dominant emission mechanism from ionised nebulae is bremsstrahlung (or free-free radiation). Due to the direct dependance of the bremsstrahlung emissivity on the square of the electron density the radio-continuum observations of PNe are an important source of information concerning the overall physical structure and mass of the ionised gas. Also, the radio brightness is especially effective as an evolutionary tracer due to its intrinsic dependence on the ionised gas density and the degree of ionisation. In the initial stage of the post-AGB evolution, the radio flux density will be proportional to the number of ionising photons from the central star (Zijlstra 1990), while from the moment when the shell becomes fully ionised, the radio-evolution starts to be governed mostly by the expansion of the ionised gas.

Targeted radio-continuum observations of PNe are usually based on optically identified objects. However, the effects of interstellar reddening, especially in directions where most PNe are expected to be found (eg. Galactic plane and Galactic bulge) have strongly biased optically detected PNe toward intrinsically radio brighter objects. The new Mac-

quarie/AAO/Strasbourg H α (MASH) catalogues of Galactic PNe (GPNe; Parker et al. 2006; Miszalski et al. 2008) have increased by nearly 40% the known population of Galactic PNe, which now stands at nearly 3000 in total (Frew & Parker 2010) and made a major impact in the domain of PNe with low and extremely low luminosities which were previously poorly represented. These significant discoveries derived from the innovative AAO/UKST SuperCOSMOS H α survey of the Southern Galactic Plane (SHS; Parker et al. 2005) whose depth, arcsecond resolution, uniformity, and 4000 square degree areal coverage opened fresh parameter discovery space.

Key problems in PN research are some of the main aims of current and future studies of the MASH team which will fully exploit this new large sample (e.g. Frew & Parker 2006; Cohen et al. 2007; Miszalski et al. 2008, 2009a,b; Kovacevic & Parker 2009). These problems include the distance problem, unravelling the optical and radio-continuum PN luminosity function from significant new samples in the Galactic Bulge (Kovacevic et al. 2010), understanding the quantitative differences in the multi-wavelength characteristics of PNe (Cohen et al. 2010) and examination of correlations between evolutionary stage and observable properties of PNe.

The radio-continuum data form an important component in the multi-wavelength evolutionary scheme for this new large sample of Galactic PNe. It enables direct calculation of electron densities, degrees of ionization and interstellar extinction in the direction of PNe. In this paper we present the newly compiled and complete database of radio-continuum detected MASH PNe.

2 RADIO-CONTINUUM IDENTIFICATIONS OF PNE FROM THE MASH CATALOGUE

Prior to the extensive radio-continuum survey of MASH PNe (Bojičić et al. in prep.) only a handful of MASH PNe objects have been observed in PNe-targeted radio-continuum surveys. Ratag & Pottasch (1991), using the Westerbork Radio Telescope (WSRT) and the Very Large Array (VLA) radio telescope, observed a large set of PN candidates selected from the IRAS Point Source catalogue and placed in the direction of the Galactic Bulge. The chosen sample is based on the far infrared selection criteria described in Pottasch et al. (1988). The authors noted that approximately 20% of observed objects were detectable at 6 cm though not all of detected objects were confirmed PNe. From that sample some eight objects have been recently identified as likely PN in SHS H α images and, after confirmatory optical spectroscopy, made their way into the MASH catalogue. Similarly, based on the [S III] λ 9532 survey of a 4 \times 4 degree field centred on the Galactic Centre, Van de Steene & Jacoby (2001) reported on \sim 100 possible identifications of PNe. For 63 PN candidates from this sample the obtained spectra appear consistent with highly reddened PN (Van de Steene & Jacoby 2001). Using the Australia Telescope Compact Array (ATCA), some 64 PN candidates were observed and 57 and 54 detected at 6 and 3 cm, respectively. The MASH catalogue contains five PNe observed in that survey from which only two have been positively detected in the radio-continuum.

On the other hand, several large-scale radio surveys like the NRAO VLA Sky Survey (NVSS; Condon et al. 1998), the Sydney University Molonglo Sky Survey (SUMSS; Bock et al. 1999; Mauch et al. 2003) and its complementary Molonglo Galactic Plane Surveys (MGPS and MGPS-2; Green et al. 1999; Murphy et al. 2007), and the Parkes-MIT-NRAO (PMN) survey (Wright et al. 1996, 1994; Griffith et al. 1994; Gregory et al. 1994) have proven to be an excellent source of PNe radio data (e.g. Condon & Kaplan 1998; Condon et al. 1999; Siódmiak & Tyłenda 2001; Morgan et al. 2003; Luo et al. 2005; Cohen et al. 2007; Umana et al. 2008; Viironen et al. 2009). These surveys form the basis for this study.

2.1 MASH PNe detected in NVSS

The NVSS is a blind radio survey that covers \sim 80% of the sky north of $\delta = -40^\circ$ at 1.4 GHz (20 cm). The detection threshold limit is \sim 2.5 mJy (for sources with angular size comparable with the FWHM of the produced synthesised beam) with positional uncertainties of the order of 7 arcsec at the survey limit (for sources brighter than 15 mJy the *rms* uncertainties are as low as 1 arcsec). The NVSS is \geq 90% complete at flux densities above 5 mJy except

near the Galactic Bulge, where, for the given flux threshold level, the catalogue completeness is estimated to be \geq 80% (Condon et al. 1998). For unresolved sources the incremental completeness is 50% at 2.5 mJy and it rises rapidly to 99% at 3.4 mJy.

Condon & Kaplan (1998) (hereafter CK98) reported detections of 680 of the 885 known PNe (listed in the Strasbourg-ESO Catalogue of Galactic Planetary Nebulae; Acker et al. 1992) with $\delta > -40^\circ$. An additional 22 known PNe and 122 PNe candidates satisfying the IR colour criteria from Preite-Martinez (1988) have been presented in Condon et al. (1999).

Another large data set of PNe radio-continuum identifications in the NVSS catalogue was presented in Luo et al. (2005) (hereafter LCY05). Based on the First Supplement to the Strasbourg-ESO Catalogue of Galactic Planetary Nebulae (Acker et al. 1996), PNe catalogued in Cappellaro et al. (2001); Kohoutek (2001, 2002); Kerber et al. (2003); Boumis et al. (2003) and on the set of 1047 positions from the preliminary MASH catalogue they identified 315 correlated radio-continuum detections.

However, from 178 objects detected from the preliminary MASH list, some 33 have been subsequently rejected as non-PN by the MASH team prior to publication of the MASH catalogue¹. Additionally, the MASH-II supplement (Miszalski et al. 2008) introduced a large set of PNe which have not been previously correlated with the NVSS catalogue. Thus, an updated cleaned list of MASH-NVSS radio identifications and fluxes is presented here for the first time.

Similarly as in LCY05, we first compared catalogued optical positions with NVSS positions. Cross-identifications between the two catalogues were considered as “possible” if the offset between the radio peak and the optical centroid was:

- less than 25 arcsec for objects with $\theta_{opt} < 25$ arcsec,
- less than $1.2 \times \theta_{opt}$ for objects with $25 \text{ arcsec} \leq \theta_{opt} < 45$ arcsec and
- less than θ_{opt} for objects with $\theta_{opt} \geq 45$ arcsec,

where θ_{opt} is the optically determined angular diameter in MASH (we will use this notation throughout this paper unless stated otherwise). All possible identifications were visually inspected using the finding charts (approximately 7 \times 7 arcmin) created from radio-continuum and H α images. The 1.4 GHz images were obtained from the NVSS postage stamp server².

The updated list of positive NVSS radio-continuum identifications now contains 201 MASH PNe. It includes 145 confirmed MASH PNe listed in LCY05 and additional 56 objects mostly from the MASH-II supplement. Furthermore, 14 radio detections from the updated list have been flagged as suspect due to the larger offset of the radio-peak position from the optical centroid or because their radio counterparts are just below the threshold level and haven’t been picked up by the NVSS cataloguing algorithm. In the later case we quote 2 mJy as a rough estimate of the flux density. All detected PNe are presented in Table 5. The first, second and

¹ Based on control evaluation of their multi-wavelength properties (see Frew & Parker 2010).

² www.cv.nrao.edu/nvss/postage.shtml

third row of Table 5 represent the official IAU PNG designation, the unique MASH catalogue identifier as described in Parker et al. (2006) and designation of the corresponding radio source from the original NVSS catalogue (Condon et al. 1998), respectively. The fourth, fifth and sixth columns contain the equatorial RAJ2000 and DECJ2000 coordinates of the radio source, and the angular offset from the catalogued optical position of the MASH PN (in arcsec), respectively. The integrated flux density, as given in the NVSS, and optically determined angular diameter are presented in columns seven and eight. All suspect detections have been designated with a preceding colon in the flux density column and no uncertainty in the radio flux is reported. The final column gives the identification key of a comment to some specifics of an object, usually found in comparison with optical imagery or, if available, in comparison with independent observational data. Full comments are given in Appendix A.

In total, only about 25% of MASH PNe have been detected in the NVSS. In this statistic we include all NVSS “detectable” MASH objects i.e. north of $\delta = -40^\circ$ and with angular diameters smaller than 100 arcsec. Of course, relatively bright objects, larger than 100 arcsec, are detectable in VLA configurations used in the NVSS (Condon et al. 1998). However, due to the generally low radio brightness of MASH PNe, we adapted 100 arcsec as a reasonable upper limit. In comparison with $\sim 75\%$ NVSS detections of known PNe (CK98) it is clear that the MASH sample contains an intrinsically radio-fainter population at 1.4 GHz than previously observed. Following the analysis given in CK98 and LCY05, we plot in Fig. 1 the number of detected sources per decade of flux density. We plot known PNe catalogued in CK98 (black-filled triangles), an updated sample of MASH PNe combined with the list of 137 non-MASH PNe from LCY05 (open circles) and the full sample (open triangles). Overplotted with filled circles is the “old” sample from LCY05 which contains non-PNe contaminants. As can be seen from Fig. 1, the distribution did not change significantly from LCY05 (see Fig. 2 in Luo et al. 2005). However, it is important to note that the number of objects with $S_{1.4\text{GHz}} < 10$ mJy increased by about 10% while almost all objects listed in LCY05 with $S_{1.4\text{GHz}} > 100$ mJy, have now been excluded from the final MASH catalogue as being PNe contaminants.

2.2 MASH PNe detected in SUMSS/MGPS-2

The SUMSS and the MGPS-2 are 35.6 cm (0.843 GHz) complementary radio surveys carried out with the Molonglo Observatory Synthesis Telescope (MOST). The main products of both surveys are $4.3'' \times 4.3''$ mosaic images with $45'' \times 45''$ cosec δ resolution making them the highest resolution large scale radio-continuum surveys of the southern Galactic plane (Mauch et al. 2003; Murphy et al. 2007).

The SUMSS catalogue is concentrated on the extragalactic radio population covering approximately 8000 square degrees with $\delta < -30^\circ$ and $|b| > 10^\circ$. The MGPS-2 is the Galactic plane counterpart to SUMSS covering the range $|b| < 10^\circ$ and $245^\circ < l < 365^\circ$. Positional uncertainties of both surveys are usually smaller than 2 arcsec. Version 2.0 of the SUMSS catalogue contains sources brighter than 6 mJy Beam $^{-1}$ at $\delta \leq -50^\circ$ and 10 mJy Beam $^{-1}$ at $\delta > -50^\circ$ with estimated errors in the internal flux density scale

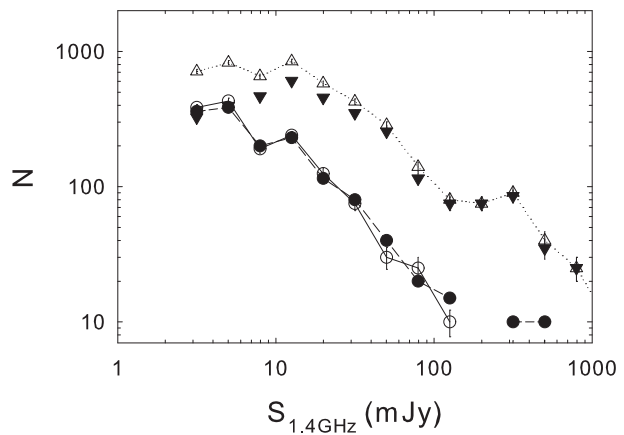


Figure 1. Numbers N of detected PNe per decade of 1.4 GHz flux density $S_{1.4\text{GHz}}$. Open circles connected with the dashed line and black-filled circles connected with the solid line represent the new MASH + 137 non-MASH PNe from LCY05 and the “old” sample from LCY05 which contains non-PNe contaminants. Black-filled triangles are known PNe from CK98. Open triangles, connected with the dotted line, represent the new full sample presented in this paper.

smaller than 3%. The sensitivity limits and flux uncertainties in the MGPS-2 catalogue are similar to SUMSS.

Selection criteria based on position, angular dimension and angular resolution, following the scheme as for NVSS (see § 2.1), are applied to these two catalogues. For visual inspection we used available total intensity images from the SUMSS postage stamp server³ (SUMSS/MGPS-2 radio-continuum images hereafter). Finding charts were composed for 527 MASH PNe positions for which SUMSS/MGPS-2 radio-continuum images were available.

None of the 13 MASH PNe with $\delta < -30^\circ$ and $|b| > 10^\circ$ are catalogued in the SUMSS catalogue. However, it should be noted that four of these 13 objects possess much larger angular diameters than the FWHM of the MOST restoring beam (965 arcsec, 401 arcsec, 420 arcsec and 250 arcsec, respectively). The other nine MASH PNe are clearly below the sensitivity limit of the SUMSS. In the first iteration, from 672 MASH PNe in the $|b| < 10^\circ$ and $245^\circ < l < 365^\circ$ region, we cross-identified 65 radio objects from the MGPS-2 catalogue. After visual inspection of finding charts, 50 objects have been assigned with a “positive detection” flag. From the rest of the preliminary list three objects were flagged as “suspect” detections and 12 objects as “non-detection”. Also, additional 28 MASH PNe have been assigned with a “possible detection” flag. Radio counterparts from the later group were found from the correlation between the optical position and an obvious flux excess over the surrounding noise. None of these objects is catalogued in the MGPS-2 catalogue. Possible detections for three of these 28 (PHR1115–6059, PHR1346–6116 and PHR1625–4522) are discussed in more details in Appendix A. The radio contour plots for other 25 possible detections are presented in Appendix A: Fig. A6 and Fig. A7. We made an initial estimate

³ <http://www.astrop.physics.usyd.edu.au/cgi-bin/postage.pl>

Table 1. The nine MASH PNe detected and possibly detected in the PMN survey.

PNG	MASH Name	PMN source	RAJ2000	DEJ2000	Offset [$''$]	S _{5GHz} [mJy]	θ_{opt} [$''$]	c.
267.4+01.3	PHR0907–4532	J0907–4532	09 07 31.2	–45 32 51	20.0	79±9	199	-
318.9+00.7	PHR1457–5812	J1457–5812	14 57 35.3	–58 12 00	9.5	80±8	27.8	-
324.3+01.1	PHR1529–5458	J1529–5458	15 29 28.9	–54 58 32	27.1	50±8	92.5	-
329.8–03.0	PHR1617–5445	J1617–5445	16 17 26.0	–54 45 36	58.8	44±8	17.4	-
333.9+00.6	PHR1619–4914	J1619–4913	16 19 38.9	–49 13 51	14.8	244±15	33.9	-
337.4+02.6	PHR1625–4522	J1625–4522	16 25 52.5	–45 22 06	37.1	165±12	314.6	-
335.4–01.9	PHR1637–4957	J1637–4958	16 37 46.3	–49 58 21	33.8	42±8	19.2	-
003.5–01.2	PPA1758–2628	J1758–2628	17 58 38.2	–26 28 55	18.0	:76±11	4.5	-
003.6–01.3	PHR1759–2630	J1759–2631	17 59 11.5	–26 31 11	47.7	:50±11	8.5	-

of flux densities for these radio objects. We used MIRIAD’s IMFIT task to fit an elliptical ($45'' \times 45'' \cdot \cos \delta$) Gaussian to all possible detections. For an estimate of cut-off noise we used a $3\sigma_{rms}$ level where σ_{rms} is the local *rms* noise level.

In order to examine the quality of the fits we also measured flux densities of all available detections from the catalogued entries. Figure 2a shows a comparison between catalogued (abscissa) and fitted (ordinate) flux densities. Three PNe with the largest offset from the catalogued flux (PHR1529-5458, PHR1517-5751 and MPA1337-5751) and the brightest object in this sample (PHR1619-4914) appear to be partially resolved in the SUMSS/MGPS-2 radio-continuum images. The divergence in flux density estimates, for resolved or partially resolved objects, are caused by the simplified fitting method we used.

As can be seen from Fig. 2a most fitted values in the 10–20 mJy region are well contained within the $\sim 20\%$ deviation from the expected (catalogued) value. However, the 90% prediction band (dotted line) in the region below 10 mJy imply that errors in our fitted flux densities could be substantial. Thus, we stress that quoted values must be taken only as rough estimates for flux densities.

Fig. 2b shows the histogram distribution of flux densities for detected and possibly detected MASH PNe. Approximately 10 objects, flagged as possible detections, have fitted flux densities above the average 10 mJy threshold level for catalogued MGPS-2 sources. Some of these objects appear to be partially resolved or to be only marginal detections (e.g. PHR1115-6059 and PHR1625-4522) and some were found in particularly noisy regions with the local noise much higher than the usual 1–1.5 mJy Beam^{−1} (e.g. PHR1619-5131) or on the top of the some larger radio structure (e.g. MPA1523-5710).

The final list of MASH PNe detected (including suspect detections) and possibly detected in SUMSS/MGPS-2 contains 53 and 28 objects, respectively. It is important to remember that for $\sim 25\%$ of MASH PNe, with positions south of $\delta = -30^\circ$, SUMSS/MGPS-2 mosaics were not available. Therefore, another ~ 10 objects could have 0.843 GHz flux densities larger than 5 mJy. All detected PNe are presented in Table 6. Possible detections are presented in Table 7. We list the PNG and MASH designations in columns 1 and 2, and the original MGPS-2 designation, if the object is catalogued, or designation produced by following the usual radio source nomenclature i.e. *JHHMMSS-DDMMSS* in the case of possible detection. Next we list RAJ2000 and DECJ2000 of the radio source (columns 3, 4 and 5, respec-

tively), the angular offset from the catalogued optical position in arcsec (column 6) and the total flux density as given in the MGPS-2 catalogue and optically determined angular diameter (columns 7 and 8). The final column gives the identification key of a comment to some specifics of an object, usually found in comparison with optical imagery or, if available, in comparison with independent observational data. Full comments are given in Appendix A.

2.3 MASH PNe detected in PMN

The PMN survey (Wright et al. 1994) fully covers the complete angular distribution of the MASH catalogue. It was made at 4.8 GHz using the NRAO multi-beam receiver mounted at the prime focus of the Parkes 64-m radio telescope. The survey was divided into four zones covering declinations between 10° to $-9^\circ.5$ (Equatorial), $-9^\circ.5$ to -29° (Tropical), -29° to -37° (Zenith) and -37° to $-87^\circ.5$ (Southern) and with approximate flux limits of 40 mJy, 42 mJy, 72 mJy and 20–50 mJy for each zone, respectively. The resolution of the survey was $4'.2$.

A preliminary list of possible detections was created from comparison between positions from the MASH and PMN catalogues. PMN radio sources within 60 arcsec from the MASH optical position have been taken into consideration. All possible detections have been examined using the total intensity maps obtained from the Australia Telescope National Facility’s (ATNF’s) FTP server⁴ for the PMN survey. Finding charts, for all detected objects, are presented in Appendix A: Figure A1.

The low resolution and the relatively low sensitivity of the PMN survey allow detection of only nine brighter objects (considering the expected low radio-continuum brightness of MASH PNe). The positive detection flag is applied to 7 MASH PNe and the suspect detection to two MASH PN. Table 1 presents the PNG and MASH designation of the detected object, PMN J2000-based source name, RAJ2000 and DECJ2000 of the radio source, offset from the MASH optical position in arcsec, flux density as published in the original catalogue, optically determined angular diameter and any comment. Suspect detections are marked with a preceding colon in the flux density column.

⁴ <ftp://ftp.atnf.csiro.au/pub/data/pmn/surveys/>

Table 2. List of MASH PNe with 5GHz detections compiled from the literature.

PNG	MASH Name	RAJ2000	DEJ2000	Offset	$S_{5\text{GHz}}$	θ_{opt}	Ref.	c.
				[$''$]	[mJy]	[$''$]		
293.1−00.0	BMP1128−6121	11 28 12.8	−61 21 02	5	34.5	7	6	-
322.2−00.7	BMP1524−5746	15 24 24.1	−57 46 21	1	39.8	7	6	-
350.4+02.0	PHR1712−3543	17 12 34.1	−35 43 17	3	12.6	10.1	1	1
350.8+01.7	MPA1714−3535	17 14 49.8	−35 35 40	0	37.2	5	1	-
344.8−02.6	MPA1715−4303	17 15 16.0	−43 03 53	1	9.6	7	6	-
355.0+02.6	PPA1722−3139	17 22 42.2	−32 30 18		43	8.5	1	-
356.0+02.8	PPA1724−3043	17 24 58.3	−30 43 04	0	5.8	4.9	2	-
000.4+04.4	PPA1729−2611	17 29 52.4	−26 11 13	0	11.4	9	1	1
000.3+04.2	PPA1730−2621	17 30 12.3	−26 21 01	0	2.3	6	1	-
353.9+00.0	PPA1730−3400	-	-		<2.5	4.5	5;7	-
353.6−02.6	PPA1740−3543	17 40 45.5	−35 43 59	2	5.8	9	1	1
356.6−01.9	PHR1745−3246	17 45 09.8	−32 46 14	3	23.1	43.2	1	1
000.1−01.7	PHR1752−2941	17 52 49.1	−29 41 55	5	4.4	13.9	3	-
000.3−01.6	PHR1752−2930	17 52 52.2	−29 30 00	1	8.5	8	3	-
004.0−00.4	PHR1756−2538	-	-		<2.5	8.4	5;7	-
010.2+02.7	PHR1758−1841	17 58 14.3	−18 41 30	3	6.1	8	4	1
007.2+00.0	PPA1801−2238	-	-		<2.5	4.5	5;7	-
015.5−00.0	PHR1818−1526	-	-		<2.5	24.6	5;7	-
026.8−00.1	MPA1840−0529	18 40 49.4	−05 29 44	1	7.5	5.9	5;7	-
028.9+00.2	PHR1843−0325	18 43 15.3	−03 25 27	1	19	9.5	5;7	-
032.5−00.0	PHR1850−0021	-	-		<2.5	12.8	5;7	-
032.5−00.3	MPA1851−0028	18 51 47.6	−00 28 31	2	4.4	13.4	7	-

References: **(1)**: Ratag et al. (1990), **(2)**: Pottasch et al. (1988), **(3)**: Van de Steene & Jacoby (2001), **(4)**: Ratag & Pottasch (1991), **(5)**: Becker et al. (1994), **(6)**: Urquhart et al. (2007), **(7)**: White et al. (2005).

2.4 Chance coincidence estimation for NVSS and MGPS-2 radio detections

In order to estimate the number of matches between MASH PNe positions and catalogued radio sources from NVSS and MGPS-2 that could arise purely by chance, we produced an off-source catalogue.

All MASH PNe positions were shifted by ± 10 arcmin in RA and DEC (4 different positions) and matched with radio positions from NVSS and MGPS-2 catalogues. Only cross-correlations within 25 arcsec (which is approximately 1/2 of the synthesised beam FWHM for both surveys) have been catalogued. The average number of chance coincidence for NVSS is 12 from 695 MASH PNe (1.5%) and 3 from 549 MASH PNe (0.5%) for the MGPS-2 catalogue. This result implies that all radio-continuum detections for the two analysed catalogues and within 25 arcsec, are highly likely to be real associations.

Due to the extremely small detection rate in the PMN we assumed that all positive correlations between MASH and PMN catalogue (seven out of nine) are likely to be real. On the other hand two PMN detections flagged as suspect (radio counterparts for MASH PNe PPA1758-2628 and PHR1759-2630) are very likely caused by chance coincidence.

2.5 Other sources of MASH radio-continuum data at 6 cm

In an attempt to compile all available radio-continuum data for MASH PNe, we examined the Vizier⁵ database of as-

tronomical catalogues (Ochsenbein et al. 2000) and also an extensive literature search was undertaken using the SIMBAD⁶ astronomical database.

For 17 MASH PNe we found reliable radio-continuum data at higher frequencies. In Table. 2 we list positions, 6 cm flux densities and optically determined angular diameters of the detected objects. As stated before, some (11) of these objects have been observed as PNe candidates by Pottasch et al. (1988), Ratag et al. (1990), Ratag & Pottasch (1991) and Van de Steene & Jacoby (2001). We also found three objects radio detected by Urquhart et al. (2007) and designated as potential massive young stellar objects (MYSOs). Finally, three objects have been detected in a “blind” radio-continuum survey of the Galactic plane (in the $-10^\circ < l < 42^\circ$, $|b| < 0^\circ.4$ region) at 6 cm (Becker et al. 1994; White et al. 2005). Another five compact ($\theta_{\text{opt}} \leq 10$ arcsec) MASH PNe are located in this region of the Galactic plane. Regarding the threshold level for detection of ~ 2.5 mJy achieved in this survey we assigned upper limits of 2.5 mJy for the flux density for these five objects (designated with a preceding < in the flux density column).

Finally, the spatial distribution of PNe from the MASH catalogue, with marked radio-detected objects, is presented in Fig. 3. NVSS, MGPS-2 and PMN detections are marked with green, yellow and red-filled circles, respectively. Other radio-continuum detections are marked with blue-filled circles. Black filled circles represent MASH PNe not detected in the radio-continuum. The “southern” part of the catalogue (the sub-sample below $\text{DEC} = -30^\circ$) is under-represented due to the lack of the radio-continuum survey of similar

⁵ <http://vizier.u-strasbg.fr/viz-bin/VizieR>

⁶ <http://simbad.u-strasbg.fr/simbad/>

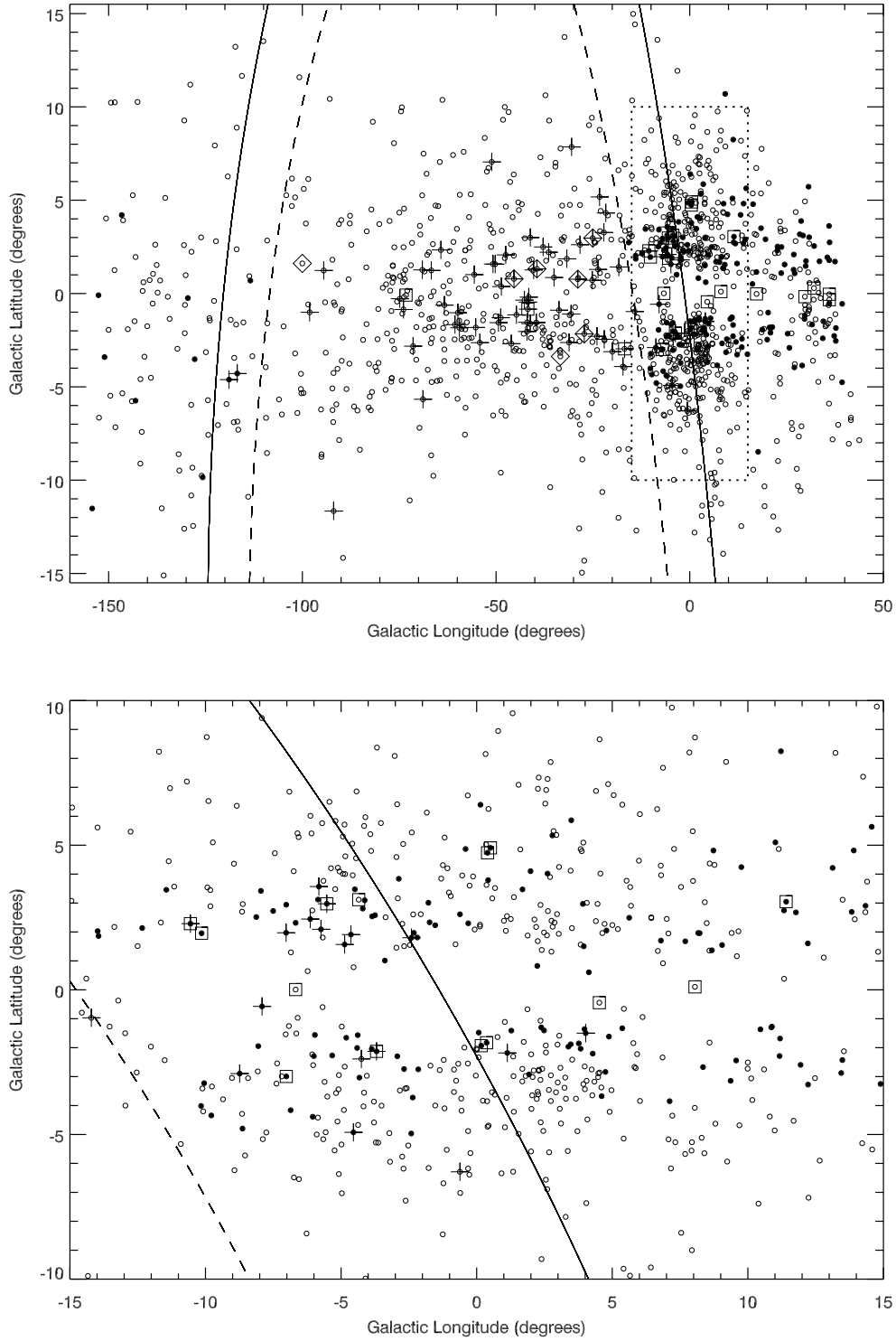


Figure 3. Galactic distribution of PNe from the MASH catalogue (empty circles) showing the full MASH sample (top panel) and the portion of the MASH sample located in the direction of the Galactic Bulge (bottom panel). NVSS, MGPS-2 and PMN detections are marked with black filled circles, crosses and diamonds, respectively. Other radio-continuum detections are marked with boxes. Continuous and dashed lines represent $\text{DEC} = -30^\circ$ and $\text{DEC} = -40^\circ$, respectively. The zoom window, centred on the position of the Galactic centre, is represented with dotted line. Note that points are plotted on top of each other where the original, empty circles, are at the lowest layer.

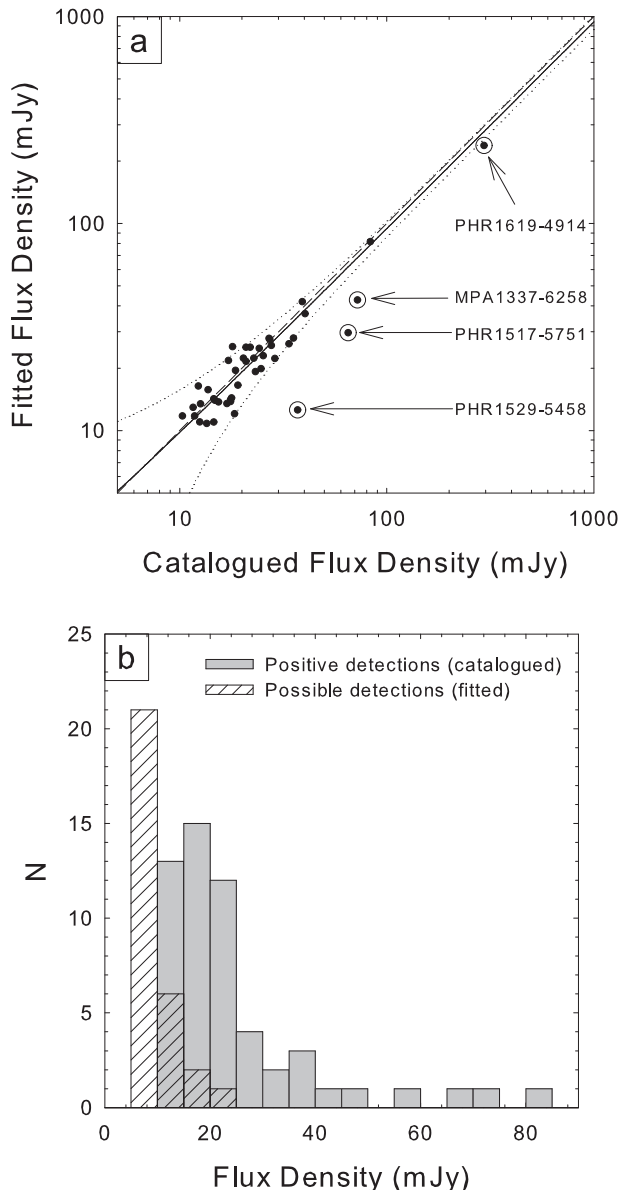


Figure 2. **a)** Comparison between catalogued (abscissa) and fitted (ordinate) 0.843 GHz flux densities. Four marked PNe (PHR1529-5458, PHR1517-5751, MPA1337-5751, PHR1619-4914) appear to be partially resolved in SUMSS/MGPS-2 radio-continuum images. The solid line represents the 1-1 relation and 90% prediction bands were plotted with dotted lines. **b)** The distribution histogram of flux densities for detected (grey filled) and possibly detected (open hatched) MASH PNe in MGPS-2.

(or better) sensitivity compared to the NVSS. While the brighter portion of MASH PNe is well covered by the MGPS-2 survey, future observational studies (Bojić et al. in prep.) will try to improve the completeness of the radio detected MASH PNe.

3 COMPARISON WITH RADIO DETECTED POPULATION OF GALACTIC PNe

The initial comparison of radio-continuum properties between previously known and new MASH PNe detected in the NVSS survey (see Fig. 1) clearly suggested that MASH planetaries do not simply present a population of PNe detectable but missed in previous surveys but are an intrinsically faint class of radio objects. The measurable, total radio-continuum emission from PNe, mainly produced in the bremsstrahlung mechanism, principally depends on the distance to the object and the mass, density stratification and chemical abundance of the ionised material. Thus, the low radio-continuum flux density of MASH PNe should be related to their spatial and/or evolutionary properties.

In order to quantitatively examine the radio-continuum properties of MASH PNe in comparison with the previously known part of the Galactic PNe population we compiled a comprehensive database of 5 GHz radio-continuum measurements of GPNe from the literature. Prior to this study two large databases of PNe radio properties were given by Acker et al. (1992) and Cahn et al. (1992). Also a number of studies used and extended these databases or presented new, refined samples, e.g. Zhang & Kwok (1993); Stasinka & Tytenda (1994); Zhang (1995); Buckley & Schneider (1995); Bensby & Lundström (2001); Siódmiak & Tytenda (2001); Phillips (2002); Urošević et al. (2009). All these samples were biased toward more accurate measurements which naturally arise from the more radio-bright PNe. Since MASH PNe clearly represents the low end of the PNe radio brightness distribution it was very important to assemble the deepest possible set of flux densities for GPNe for comparison.

We restricted our search to 5 GHz (6 cm) observations because at this frequency most PNe are optically thin so the observed flux reflects the intrinsic physical properties of the ionised nebula (assuming that a valid distance determination can be achieved). Also, the expected background radiation is weaker than at lower frequencies and so the possible confusion with nearby sources is less (this property is especially important for the data obtained via single-dish observations). These two assets of high frequency radio observations of PNe are in fact the major reason why the majority of PNe targeted surveys were performed at 5 GHz. We based our literature search on the Kerber et al. (2003) catalogue of accurate positions of 1312 Galactic PNe originally listed in the Strasbourg ESO Catalogue, its supplement and version 2000 of the Catalogue of Planetary Nebulae as well as the new 2 kpc volume limited sample of Frew (2008) (hereafter F08). All radio detections have been traced to the original observational data or to the first citation. If more than one observation was available, and results from different sources appear to be in agreement, we used a simple average between reported values. Interferometric data were preferred over the single-dish measurements, except in the case of objects with quoted large angular sizes (two or more times larger than the FWHM of a synthesised beam). Secondly, results from targeted surveys were preferred over results from “blind” surveys.

The majority of flux densities in the compiled catalogue originate from the VLA surveys of Zijlstra et al. (1989) and Aaquist & Kwok (1990) (~ 50%) and the Parkes radio

Table 3. PN impostors found in current radio catalogues.

Name	θ_{opt} ["]	S _{6cm} [mJy]	Type	Ref.
Abell 35	772.0	255.0	Bowshock neb?	1
Ns 238	56.0	4173.0	compact HII	2
M 1-67	120.4	198.0	Pop I WR shell	3
PHL 932	270.0	10.0	HII region	4
Mz 3	32.9	649.0	B[e] or Sy*	5, 6, 7
He 2-146	34.2	186.0	compact HII	6
PP 40	30.0	213.0	compact HII	3
M 2-9	20.2	36.0	B[e] or Sy*	5
FP0840-5754	339.9	18.4	HII region?	8
PHR1517-5751	104.2	54.7	HII region	8

References: 1: Frew (2008); 2: Copetti et al. (2007); 3: Kohoutek (2001); 4: Frew et al. (2010); 5: Frew & Parker (2010); 6: Cohen et al. (2010); 7: Kastner et al. (2003); 8: Parker et al. (2010), in preparation.

telescope surveys of Milne & Aller (1975) and Milne (1979) ($\sim 20\%$). The full catalogue of ~ 600 Galactic PNe for which we found reliable 5 GHz flux densities will be presented in a future paper.

Note that a number of emission nebulae that are often classified as PN in the literature have been excluded from Fig. 4. In Table 3 we list these objects, giving the correct classification and a reference from the literature justifying why each is a probable PN mimic (Frew & Parker 2010).

3.1 The $S_\nu - \theta$ evolutionary diagram

In Fig. 4 we compare the positions of radio detected Galactic PNe in the flux density (S_ν) versus angular diameter (θ) plot. This plot essentially represents a radio-evolutionary diagram (Kwok 1985; Zijlstra 1990) of a mixture of PNe at different distances and with a variety of intrinsic physical properties (mostly related to the mass of the progenitor star).

The 5 GHz flux densities of ~ 600 previously known Galactic PNe are plotted with grey-filled circles and then overplotted with the 84 radio detected PNe within the 2 kpc volume limited sample (F08; black-filled boxes). Since we found only a limited number of 5 GHz detections for MASH PNe we estimated 5 GHz flux densities from low frequency measurements (i.e. from 1.4 GHz and 0.843 GHz flux densities reported in NVSS and MGPS-2 catalogues, respectively) using equations 2 and 6 (see § 4) and adopting the canonical electron temperature of 10^4 K for all MASH PNe. The adopted method accounts for the radio optical thickness effect only to some extent because it uses the same (optically determined) angular diameter in both the optically thick and optically thin regime. If a MASH PN is detected in both the NVSS and MGPS-2 surveys we used the flux density from the 1.4 GHz observation. The calculated 5 GHz flux densities versus optically determined angular diameters, for some 210 radio-continuum detected MASH PNe are plotted with black dots.

The difference in distances can be roughly seen from comparison of PNe positions at lines of constant brightness temperature (T_b). T_b is a distance independent evolutionary property of the evolving ionised nebulosity such that the

changing distance to objects can only displace the position of an object in the $S_\nu - \theta$ diagram along a line of constant T_b (Zijlstra 1990). Assuming a simple, constant expansion velocity of a spherically symmetric, constant density and fully ionised nebula, the optically thin flux density S_ν , at a distance D , will be related to its angular diameter θ as (Daub 1982):

$$S_\nu \propto \theta^{-3} D^{-5} \quad (1)$$

In Fig. 4 lines of constant T_b were plotted with dashed lines. The simplified evolutionary tracks, calculated from eq. 1 at 1 kpc, 2 kpc and at the mean distance of the Galactic Bulge (7.9 kpc; Eisenhauer et al. 2003) were plotted with dotted lines.

It is important to note that the presented radio evolution of PNe is clearly a strong simplification of the real picture. It doesn't account for the optically thick phase ($T_b > 10^3$ K), density and temperature gradients, and assumes an uniform expansion of a spherically symmetric and fully ionised nebular shell around the non-evolving central star (CS). In the more realistic case the CS and nebular properties are changing mutually. The gas density stratification in a PN is far from constant and it will continue to change during the subsequent evolution because of the energy-input from the fast wind and due to the progress of the strong ionisation front throughout the neutral gas. Thus, the optical depth at 5 GHz can be important in the initial stage of the PN evolution. Also, the episode in CS evolution in turning to the “cooling path” could result in recombination in denser nebular regions and cause a drastic drop in the radio flux. However, the goal of this paper is not to provide a complete description of the radio-continuum emissivity from the evolving CS-PN system. We believe that the used simplifications do not corrupt our preliminary analysis of the evolutionary position of radio detected MASH PNe in comparison with local and general radio detected Galactic PN populations.

From the presented radio-evolutionary diagram (Fig. 4) a clear separation between the local volume sample (F08) and the rest of the Galactic PNe population can be seen supporting the general reliability of the Frew (2008) distances. In the region above $T_b = 100$ K, evolutionary tracks for PNe at 1 kpc and 2 kpc start to strongly diverge from the empirical distribution mostly because, as stated before, we used approximations of negligible self-absorption and fully ionised nebulae. The highly discrepant F08 object in Figure 4 is KJpN 8 (Lopez et al. 1995). This very unusual object appears not to be a conventional PN (see Frew & Parker 2010, for a discussion). The compact, PN-like core (detected at 6 cm) is surrounded by a very large, shock-excited, bipolar nebula, which has an emission measure too low to have been detected in extant radio surveys. The small core is very underluminous at both optical and radio wavelengths at the accepted distance of 1.6 kpc (Meaburn 1997), falling off the $H\alpha$ surface brightness – radius relation (Frew & Parker 2006, 2010).

More importantly, we can also see a gradual increase in the number of MASH PNe below $T_b \approx 100$ K and with no MASH objects with brightness temperatures above that value. If MASH PNe follow the same central star mass distribution as the rest of the GPNe population then this implies

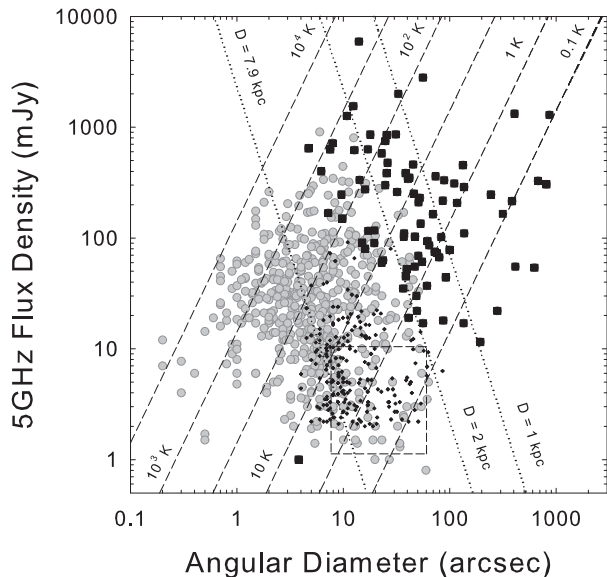


Figure 4. Distribution of the catalogued sample of Galactic PNe in the $S_\nu - \theta$ diagram. Grey-filled circles and black dots represents the previously known and new MASH samples, respectively (see text for more details). Black-filled boxes represent the 2 kpc volume limited sample from F08. The discrepant point in the F08 sample plotted near the bottom is KJpN 8 (see text for details). Levels of constant brightness temperature are shown as dashed lines. Evolutionary tracks at 1, 2 and 7.9 kpc are plotted with dotted lines. The dashed-line rectangle presents the initial estimate of the region where we expect to improve completeness of the GPNe sample with our new ATCA high-frequency observations (Bojčić et al. in prep.).

that the MASH samples do not contain (at least not a significant number) young PNe and that radio “faintness” is strictly correlated to evolutionary properties. However, we cannot eliminate the possibility that some of these nebulae are related to low-mass central stars ($M_{CS} < 0.6 M_\odot$). In that case the ejected layers of gas could already be highly dispersed at the point when the central star increases the effective temperature enough to produce a significant number of photons in the Lyman continuum. The starting point in the T_b evolution of these PNe will be way below $10^3 - 10^4$ K as expected for “normal” PNe.

The expected excess of the number of low brightness PNe around 7.9 kpc can also be seen. Obviously, the large density of MASH PNe along the 7.9 kpc evolutionary track is mostly caused by sampling bias. As we mentioned before the NVSS fully covers the bulge region, where the concentration of MASH PNe is the largest, while the southern sample is only covered above 10 mJy with the MGPS-2.

3.2 The radio surface brightness distribution

In order to strengthen our claim of intrinsic low radio luminosity of MASH PNe we also examined their position in the radio brightness temperature distribution diagram. The radio brightness temperature, as a distance independent parameter, is a valuable evolutionary tracer especially after the shocked shell becomes fully ionised, when T_b will start

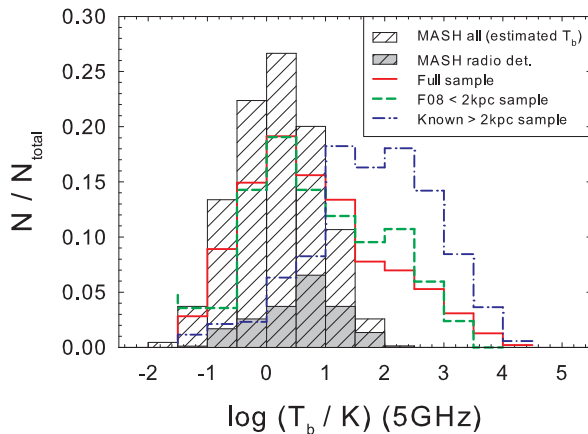


Figure 5. The 5 GHz brightness temperature distribution of selected samples of Galactic PNe. Grey hatched and white hatched histograms represent the detected and detected + undetected (see text for more details) MASH PNe, respectively. The green dashed line represents the T_b distribution of 84 radio detected PNe from the 2 kpc volume limited sample (F08), the blue dash-dotted line represents the sample of radio detected Galactic PNe excluding the 2 kpc volume limited sample and the red solid line is the distribution of the full sample (known + MASH detected and undetected). All distributions were normalised to the total number of elements in the corresponding sample except for the radio detected MASH sample which is normalised to the total number of PNe in the detected + undetected sample. (This figure is in colour in the online version of the Journal.)

to evolve toward lower values due to the consequent nebular expansion.

We calculated the radio surface brightness temperatures at 5 GHz for PNe in selected samples: previously known Galactic PNe at distances > 2 kpc (521 objects; i.e. excluding F08 sample), F08 sample (84 objects), positively radio detected MASH PNe (175 objects; possible detections were not included) and “radio-undetected” MASH PNe (631 objects). MASH PNe designated as “true” and with optically determined angular diameters $\theta_{opt} < 100$ arcsec were selected for this analysis. With assumption of a negligible optical depth at 1.4 GHz and 0.843 GHz we used the detection limits from NVSS and MGPS-2 to estimate 5 GHz flux densities for “radio-undetected” MASH PNe. For objects with declinations $\delta \geq -40^\circ$ and $\delta < -40^\circ$ we used $2.5 \times (4.8/1.4)^{-0.1}$ mJy Beam $^{-1}$ and $10 \times (4.8/0.843)^{-0.1}$ mJy Beam $^{-1}$, respectively. The resulting histogram for comparison between selected samples is presented in Fig. 5.

The distinction between known and MASH PNe is even more evident from this diagram. No more than 12% of PNe from the MASH catalogue were placed within the brightest three magnitudes of the $\log(T_b)$ distribution. The radio detected MASH PNe sub-sample shows a peak at $\log(T_b) < 1$ which is the position of the significant drop in the distribution of known PNe (> 2 kpc sample). This strongly implies that MASH PNe are the evolutionary complement of the previously known Galactic PNe. The concentration of radio-undetected MASH PNe, which is propagated to the distribution of the full sample (red solid line), around $\log(T_b) \approx 0$ is artificial and caused by placing of flux densities of this large

Table 4. Spectral indices of multi-wavelength radio-continuum detected MASH PNe. The averaged spectral index between frequencies ν_1 and ν_2 (α_{ν_1/ν_2}^*) is calculated using eq. 2. Values of α_{ν_1/ν_2}^* calculated from an unreliable flux density (upper/lower limit or possible detection) are designated with a preceding colon.

Name	$\alpha_{0.843/1.4}^*$	$\alpha_{0.843/5}^*$	$\alpha_{1.4/5}^*$
PHR0748–3258	0.5 ± 0.2	-	-
PHR0754–3444	-0.3 ± 0.2	-	-
PHR1457–5812	-	0.0 ± 0.1	-
BMP1524–5746	-	0.2 ± 0.1	-
PHR1529–5458	-	-0.2 ± 0.1	-
PHR1619–4914	-	-0.11 ± 0.05	-
PHR1637–4957	-	0.1 ± 0.1	-
PHR1712–3543	0.0 ± 0.3	0.0 ± 0.1	0.0 ± 0.1
MPA1714–3535	-	-	0.5 ± 0.1
MPA1715–4303	-	-0.3 ± 0.1	-
PHR1719–3134	-2.6 ± 0.5	-	-
PPA1722–3317	-0.5 ± 0.3	-	-
PPA1722–3139	0.6 ± 0.3	0.5 ± 0.1	0.4 ± 0.1
PPA1723–3223	-0.8 ± 0.6	-	-
PPA1725–3216	-1.1 ± 0.4	-	-
MPA1728–3132	-0.7 ± 0.6	-	-
PPA1729–3152	-0.7 ± 0.4	-	-
MPA1729–3513	0.5 ± 0.2	-	-
PPA1729–2611	-	-	0.0 ± 0.1
PPA1730–2621	-	-	-0.2 ± 0.4
PPA1734–2954	-0.1 ± 0.3	-	-
PHR1736–3659	-0.1 ± 0.3	-	-
PPA1740–3543	-	-	0.2 ± 0.2
PHR1745–3246	-0.2 ± 0.2	-0.2 ± 0.1	-0.2 ± 0.1
PHR1752–2941	-	-	0.3 ± 0.3
PHR1752–2930	-	-	0.6 ± 0.1
PHR1753–3443	-0.6 ± 0.2	-	-
PHR1755–2904	-2.3 ± 0.4	-	-
PHR1758–1841	-	-	-0.9 ± 0.2
PPA1758–2628	-	-	1.4 ± 0.1
PHR1759–2630	0.7 ± 0.2	0.2 ± 0.1	0.0 ± 0.2

set of PNe at the detection limits. Thus, it is more likely that the real distribution will have a much milder gradient or even settling to a constant level at $\log(T_b) < 1.5$.

4 A PRELIMINARY RADIO-CONTINUUM SPECTRAL ANALYSIS OF MASH PNE

Finally, using the newly collected data-set, we examined the radio-continuum spectral properties of a small sub-set of multi-wavelength radio-continuum detected MASH PNe.

The averaged spectral index α_{ν_1/ν_2}^* between measured flux densities S_{ν_1} and S_{ν_2} at frequencies ν_1 and ν_2 can be found from:

$$\alpha_{\nu_1/\nu_2}^* = \frac{\ln(S_{\nu_1}/S_{\nu_2})}{\ln(\nu_1/\nu_2)} \quad (2)$$

and it will vary between -0.1 and 2 i.e. between cases when radio-continuum emission at both frequencies is optically thin or optically thick, respectively. Table 4 lists spectral indices for 33 MASH PNe for which we found flux densities at more than one frequency. Values of α_{ν_1/ν_2}^* calculated from

an unreliable flux density (upper/lower limit or possible detection) are designated with a preceding colon.

It is important to note that comparison of flux densities obtained with different instruments must take in to account a range of spatial frequencies which could be present in the observed source and which could be successfully measured by the used radio telescope. This is especially important when comparing single dish and interferometric measurements of the faint and extended source (comparing to the FWHM of the interferometer's synthesised beam; Pottasch & Zijlstra 1994). While the spectral indices between 1.4 GHz and 0.843 GHz (NVSS and MGPS-2) were obtained from flux measurements with the matching synthesised beam size, the 5 GHz flux densities originate from single-dish and interferometric radio observations ranging in resolution from $4''.2$ (PMN) to $2''$ (ATCA in the 6A configuration). Except for PHR1529-5358 ($\theta_{opt} = 114$ arcsec), for which we already marked the 0.843 GHz flux density as suspect, the rest of the PMN detected sub-sample is comparable or much smaller than the NVSS and MGPS-2 synthesised beams. Thus, we believe that our comparison of NVSS and MGPS-2 flux densities with those from PMN is valid. However, we stress that the accuracy of spectral indices obtained from comparison of NVSS and MGPS-2 flux densities with those from interferometric observations could suffer from filtering out of flux from larger structures and should be taken with caution.

Assuming that the observed radiation at ν_1 and ν_2 is coming from the same solid angle, the S_{ν_1}/S_{ν_2} ratio can be calculated from (Siódmiak & Tyłenda 2001):

$$\frac{S_{\nu_1}}{S_{\nu_2}} = \left(\frac{\nu_1}{\nu_2}\right)^2 \frac{1 - e^{-\tau_{\nu_1}}}{1 - e^{-\tau_{\nu_2}}} \quad (3)$$

The optical depth through the ionised envelope, at frequency ν_1 , can be approximated with (Pottasch 1984):

$$\tau_{\nu_1} = 8.235 \times 10^{-2} \left(\frac{T_e}{K}\right)^{-1.35} \left(\frac{\nu_1}{\text{GHz}}\right)^{-2.1} \left(\frac{E}{\text{cm}^{-6} \cdot \text{pc}}\right), \quad (4)$$

where E is the emission measure in $\text{cm}^{-6} \cdot \text{pc}$. Thus, at frequency ν_2 , the optical depth will be:

$$\tau_{\nu_2} = \tau_{\nu_1} (\nu_2/\nu_1)^{-2.1} \quad (5)$$

With the usual adopted approximations it can be proved that:

$$\alpha_{\nu_1/\nu_2}^* = 2 - \frac{2.1}{\ln \gamma} \ln \frac{1 - \xi^\gamma}{1 - \xi}, \quad (6)$$

where $\xi = 1 - T_e/T_b$ and $\gamma = (\nu_1/\nu_2)^{-2.1}$.

Figure 6 shows positions of these objects in $\alpha_{\nu_1/\nu_2}^* = f(T_b)$ diagrams. Only data-points with positive detections and catalogued flux densities were plotted (i.e. we did not use our estimates for 0.843 GHz flux densities). Overplotted (gray crosses) are positions of previously known PNe. The expected values for $T_e = 0.5 \times 10^4$ K, $T_e = 1.0 \times 10^4$ K and $T_e = 1.5 \times 10^4$ K are plotted with dashed, full and dotted lines, respectively.

On a first glance, comparing to the sample of previously

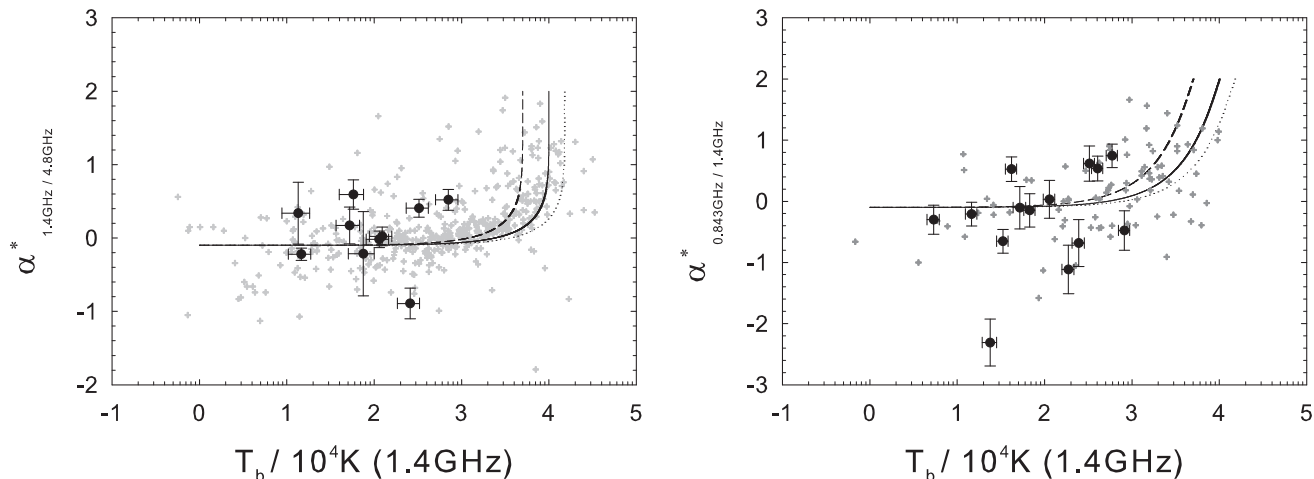


Figure 6. A plot of α^* vs. T_b at 1.4 GHz (black dots with error bars) values for MASH PNe with both available 1.4 GHz and 5 GHz flux densities (*left*) and with available 0.843 GHz and 1.4 GHz flux densities (*right*). Overplotted are data-points from the catalogue of previously known PNe. Predictions from the model are shown with a dashed line ($T_e = 5 \times 10^3$ K), solid line ($T_e = 10 \times 10^3$ K) and dotted line ($T_e = 15 \times 10^3$ K.)

known PNe, it appears that MASH PNe display larger scatter around the theoretical model. However, it is just as likely an effect of a small and generally fainter sample. We do not see a strong systematic effect in divergence from the theoretical curve and if plotted with the same symbols as the sample of previously known PNe the sub-sample of MASH PNe are practically indistinguishable. We examined several objects with apparent steep negative radio-continuum spectra, uncommon for PNe, in more detail in Appendix B.

5 SUMMARY

In this paper we present freshly compiled and re-examined radio-continuum data for MASH PNe. In searching for radio-detections we examined three large “blind” radio-continuum surveys: NVSS, SUMSS/MGPS-2 and PMN. In the most sensitive survey of these three (NVSS with detection threshold level of about 2.5 mJy) we found radio counterparts for 201 MASH PNe (25%). This number fell significantly, to 81 positive and possible detections (10%), for the southern part of the MASH catalogue covered with MGPS-2 (with catalogue detection threshold level of about 10 mJy). The radio detection rates of MASH PNe are considerably smaller than what we see for the previously known population (of about 75% and 50% for NVSS and MGPS-2, respectively).

Also, as we can see from the $S_\nu - \theta$ plot (Fig. 4) and radio brightness temperature distribution (Fig. 5), radio detected MASH PNe are concentrated at the faint end of the current PN radio-continuum brightness distribution and appear to be the evolutionary complement of the previously known Galactic PNe. This finding poses an important question: where, in these two evolutionary diagrams, should we expect to see the rest of the MASH PNe? We believe that our deep ATCA observations (Bojić et al. in prep.) at least partially answers this question.

Finally, we examine, in some detail, radio continuum

spectral properties of several MASH PNe with available multi-wavelength radio data. Except for five objects from this sub-sample, for which we found a divergence from the expected radio-continuum spectral distribution (a steep negative radio-continuum spectra), we didn’t find any strong evidence that radio-detected MASH PNe differ in radio-continuum spectral properties from their previously known “cousins”.

ACKNOWLEDGEMENTS

We used the MIRIAD software package developed by the ATNF and the Karma software package developed by Richard Gooch (Gooch 1996). This research has made use of the SIMBAD database and VizieR catalogue access tool, operated at CDS, Strasbourg, France. This research has been supported by the International Macquarie University Research Scholarship (iMURS) and University of Western Sydney research grant (project number **20721.80758**). The authors thank the referee for helpful comments that significantly improved this paper.

REFERENCES

- Aaquist O. B., Kwok S., 1990, A&AS, 84, 229
- Acker, A., Marcout, J., Ochsenbein, F., Stenholm, B., & Tyllenda, R. 1992, Strasbourg-ESO Catalogue of Galactic Planetary Nebulae, Garching: European Southern Observatory
- Becker R. H., White R. L., Helfand D. J. and Zoonematkermani S., 1994, ApJS, 91, 347
- Bensby T., Lundström I., 2001, A&A, 374, 599
- Bock D. C.-J., Large M. I., Sadler E. M., 1999, AJ, 117, 1578
- Boumis P., Paleologou E. V., Mavromatakis F., Papamastorakis J., 2003, MNRAS, 339, 735

- Buckley D., Schneider S. E., 1995, *ApJ*, 446, 279
- Cahn J. H., Kaler J. B., Stanghellini L., 1992, *A&AS*, 94, 399
- Cappellaro E., Sabbadin F., Benetti S., Turatto M., 2001, *A&A*, 377, 1035
- Cohen M., Parker Q. A., Green A. J. et al., 2007, *ApJ*, 669, 343
- Cohen M., Parker Q., Green A., Miszalski B., Frew D. J., Murphy T., 2010, **submitted to MNRAS**.
- Condon J. J., Cotton W. D., Greisen E. W., Yin Q. F., Perley R. A., Taylor G. B., Broderick J. J., 1998, *AJ*, 115, 1693
- Condon J. J., Kaplan D. L., 1998, *ApJS*, 117, 361
- Condon J. J., Kaplan D. L., Terzian Y., 1999, *ApJS*, 123, 219
- Copetti M. V. F., Oliveira V. A., Riffel R., Castañeda H. O., Sanmartim D., 2007, *A&A*, 472, 847
- Daub C. T., 1982, *ApJ*, 260, 612
- DePew K., Parker Q., Miszalski B., De Marco O., Frew D. J., Acker A., Kovacevic A., Sharp R., 2010, **submitted to MNRAS**.
- Eisenhauer F., Schödel R., Genzel R., Ott T., Tecza M., Abuter R., Eckart A., Alexander T., 2003, *ApJ*, 597, L121
- Frew D., 2008, PhD thesis, Macquarie University
- Frew, D. J., Madsen, G. J., O'Toole, S. J., & Parker, Q. A. 2010, *PASA*, 27, 203
- Frew, D. J., & Parker, Q. A. 2006, *Planetary Nebulae in our Galaxy and Beyond*, *IAUS*, 234, 49
- Frew D. J., Parker Q. A., 2010, *PASA*, 27, 129
- Gooch, R. 1996, *Astronomical Data Analysis Software and Systems V*, 101, 80
- Green A. J., Cram L. E., Large M. I., Ye T., 1999, *ApJS*, 122, 207
- Gregory P. C., Vavasour J. D., Scott W. K., Condon J. J., 1994, *ApJS*, 90, 173
- Griffith M. R., Wright A. E., Burke B. F., Ekers R. D., 1994, *ApJS*, 90, 179
- Kastner J. H., Balick B., Blackman E. G., Frank A., Soker N., Vrtílek S. D., Li J., 2003, *ApJ*, 591, L37
- Kerber F., Mignani R. P., Guglielmetti F., Wicenec A., 2003, *A&A*, 408, 1029
- Kohoutek L., 2001, *A&A*, 378, 843
- Kohoutek L., 2002, *Astronomische Nachrichten*, 323, 57
- Kovacevic, A., & Parker, Q. 2009, *Astronomical Society of the Pacific Conference Series*, 404, 337
- Kovacevic A., Parker Q., Jacoby G., Sharp R., Miszalski B., Frew D. J., 2010, **submitted to MNRAS**.
- Kwok S., 1985, *ApJ*, 290, 568
- Lopez J. A., Vazquez R., Rodriguez L. F., 1995, *ApJ*, 455, L63
- Luo S. G., Condon J. J., Yin Q. F., 2005, *ApJS*, 159, 282
- Mauch T., Murphy T., Buttery H. J., Curran J., Hunstead R. W., Piestrzynski B., Robertson J. G., Sadler E. M., 2003, *MNRAS*, 342, 1117
- Meaburn J., 1997, *MNRAS*, 292, L11
- Milne D. K., 1979, *A&AS*, 36, 227
- Milne D. K., Aller L. H., 1975, *A&A*, 38, 183
- Miszalski B., Acker A., Moffat A. F. J., Parker Q. A., Udalski A., 2009a, *A&A*, 496, 813
- Miszalski, B., Acker, A., & Parker, Q. A. 2008, *Hydrogen-Deficient Stars*, 391, 181
- Miszalski B., Acker A., Parker Q. A., Moffat A. F. J., 2009b, *A&A*, 505, 249
- Miszalski B., Parker Q. A., Acker A., Birkby J. L., Frew D. J., Kovacevic A., 2008, *MNRAS*, 384, 525
- Morgan D. H., Parker Q. A., Cohen M., 2003, *MNRAS*, 346, 719
- Murphy T., Mauch T., Green A., Hunstead R. W. and Piestrzynska B., Kels A. P., Sztajer P., 2007, *MNRAS*, 382, 382
- Ochsenbein F., Bauer P., Marcout J., 2000, *A&AS*, 143, 23
- Parker Q. A., Acker A., Frew D. J. et al., 2006, *MNRAS*, 373, 79
- Parker Q. A., Phillipps S., Pierce M. J. et al., 2005, *MNRAS*, 362, 689
- Phillips J. P., 2002, *ApJS*, 139, 199
- Pottasch, S. R. 1984, *Astrophysics and Space Science Library*, 107
- Pottasch S. R., Olling R., Bignell C., Zijlstra A. A., 1988, *A&A*, 205, 248
- Pottasch S. R., Zijlstra A. A., 1994, *A&A*, 289, 261
- Preite-Martinez A., 1988, *A&AS*, 76, 317
- Ratag M. A., Pottasch S. R., 1991, *A&AS*, 91, 481
- Ratag M. A., Pottasch S. R., Zijlstra A. A., Menzies J., 1990, *A&A*, 233, 181
- Siódmiak N., Tylanda R., 2001, *A&A*, 373, 1032
- Stasinka G., Tylanda R., 1994, *A&A*, 289, 225
- Umana G., Leto P., Trigilio C., Buemi C. S., Manzitto P., Toscano S., Dolei S., Cerrigone L., 2008, *A&A*, 482, 529
- Urošević, D., Vukotić, B., Arbutina, B., Ilić, D., Filipović, M., Bojičić, I., Segan, S., & Vidojević, S. 2009, *A&A*, 495, 537
- Urquhart J. S., Busfield A. L., Hoare M. G., Lumsden S. L., Clarke A. J., Moore T. J. T., Mottram J. C., Oudmaijer R. D., 2007, *A&A*, 461, 11
- Van de Steene G. C., Jacoby G. H., 2001, *A&A*, 373, 536
- Viironen K., Greimel R., Corradi R. L. M. et al., 2009, *A&A*, 504, 291
- White R. L., Becker R. H., Helfand D. J., 2005, *AJ*, 130, 586
- Whiteoak J. B. Z., 1992, *MNRAS*, 256, 121
- Wright A. E., Griffith M. R., Burke B. F., Ekers R. D., 1994, *ApJS*, 91, 111
- Wright A. E., Griffith M. R., Burke B. F., Ekers R. D., 1996, *VizieR Online Data Catalog*, 8038, 0
- Zhang C. Y., 1995, *ApJS*, 98, 659
- Zhang C. Y., Kwok S., 1993, *ApJS*, 88, 137
- Zijlstra A. A., 1990, *A&A*, 234, 387
- Zijlstra A. A., Pottasch S. R., Bignell C., 1989, *A&AS*, 79, 329

Table 5: MASH PNe detected in the NVSS.

PNG	MASH Name	NVSS source	RAJ2000	DEJ2000	Offset [$''$]	S _{1.4GHz} [mJy]	θ_{opt} [$''$]	c.
209.1−08.2	PHR0615−0025	061521−002544	06 15 21.25	−00 25 44.9	13.4	21.1±0.8	100	1
214.2−02.4	PHR0645−0217	064504−021739	06 45 04.09	−02 17 39.8	15.1	2.5±0.5	50.5	1
212.6−00.0	PHR0650+0013	065040+001341	06 50 40.45	+00 13 41.6	1.8	5.4±0.5	42	-
222.8−04.2	PHR0654−1045	065413−104533	06 54 13.26	−10 45 33.8	4.7	2.7±0.5	20.8	-
219.1+03.0	MPA0713−0405	071347−040521	07 13 47.93	−04 05 21.3	13.3	10.5±0.5	62.8	-
240.6−07.7	BMP0715−2805	071502−280541	07 15 02.35	−28 05 41.5	2.6	2.3±0.5	19	-
239.3−02.7	PHR0731−2439	073200−243916	07 32 00.35	−24 39 16.4	16.1	4.0±0.7	19	1
222.5+07.6	BMP0736−0500	073623−050001	07 36 23.02	−05 00 01.9	18.0	:2.7	69.6	20
237.6−00.1	BMP0738−2155	073806−215529	07 38 06.36	−21 55 29.4	2.5	3.1±0.5	10	-
247.5−04.7	PHR0742−3247	074219−324713	07 42 19.84	−32 47 13.9	56.7	:3.8	166.2	21
248.3−03.6	PHR0748−3258	074832−325821	07 48 32.08	−32 58 21.3	5.3	23.5±0.9	22.5	-
250.5−03.4	PHR0754−3444	075455−344408	07 54 55.83	−34 44 08.5	1.7	21.2±1.6	59.5	-
254.5−02.7	PHR0808−3745				-	:2.0	173.9	22
254.1+00.5	BMP0820−3536	082050−353554	08 20 50.76	−35 35 54.0	8.3	3.3±0.6	11	-
345.8+02.4	MPA1656−3912	165640−391226	16 56 40.80	−39 12 26.3	13.4	4.9±0.8	4	-
347.4+01.8	PHR1704−3819	170416−381957	17 04 16.89	−38 19 57.8	3.0	4.6±0.6	22.7	-
347.4+01.6	PPA1704−3824	170459−382412	17 04 59.32	−38 24 12.6	9.0	5.6±0.6	7.7	-
349.6+03.1	PHR1706−3544	170601−354437	17 06 01.23	−35 44 37.8	8.2	3.6±0.5	53.5	-
348.8+01.9	PPA1708−3705	170823−370544	17 08 23.38	−37 05 44.4	8.4	3.4±0.5	5.7	-
350.4+02.0	PHR1712−3543	171234−354317	17 12 34.02	−35 43 17.6	2.4	12.9±0.6	10.1	1
350.8+01.7	MPA1714−3535	171449−353541	17 14 49.58	−35 35 41.4	3.0	19.6±0.8	5	-
352.8+03.0	PPA1715−3313	171510−331351	17 15 10.65	−33 13 51.6	4.8	2.5±0.5	6.5	-
352.6+02.2	PPA1717−3349	171756−334926	17 17 56.28	−33 49 26.0	1.4	3.7±0.5	7.5	10
353.2+02.4	PPA1718−3315	171844−331526	17 18 44.54	−33 15 26.0	4.9	7.5±0.6	8	-
353.6+02.6	MPA1719−3247	171910−324718	17 19 10.83	−32 47 18.4	9.2	3.3±0.5	7.5	-
354.7+03.2	PHR1719−3134	171954−313443	17 19 54.53	−31 34 43.8	7.1	3.9±0.5	6.7	-
354.7+02.8	PPA1721−3149	172123−314952	17 21 23.89	−31 49 52.3	2.4	5.9±0.6	7.9	-
353.9+02.0	PHR1722−3251	172213−325116	17 22 13.09	−32 51 16.7	9.6	6.1±0.6	28.8	-
353.6+01.7	PPA1722−3317	172235−331714	17 22 35.43	−33 17 14.6	0.6	14.6±0.7	4	-
355.0+02.6	PPA1722−3139	172240−313956	17 22 40.85	−31 39 56.9	2.0	26.1±0.9	8.5	-
354.4+02.2	PPA1723−3223	172304−322309	17 23 04.22	−32 23 09.4	0.7	7.1±0.6	9.4	-
355.9+03.1	PPA1723−3038	172323−303840	17 23 23.47	−30 38 40.3	0.5	10.1±0.6	4	-
000.1+05.7	PHR1724−2543	172404−254328	17 24 04.47	−25 43 28.4	14.6	3.9±0.6	10.5	-
354.8+01.8	PPA1725−3216	172515−321608	17 25 15.80	−32 16 08.9	2.5	10.0±0.6	6.9	-
356.2+02.7	MPA1725−3033	172532−303410	17 25 32.33	−30 34 10.8	19.5	2.8±0.5	5	-
357.4+03.4	PPA1725−2915	172554−291510	17 25 54.45	−29 15 10.3	2.4	2.4±0.5	9	-
356.2+02.5	PPA1726−3045	172623−304536	17 26 23.61	−30 45 36.8	2.2	12.7±1.2	4.5	-
359.6+04.3	PPA1727−2653	172758−265351	17 27 58.14	−26 53 51.1	7.0	2.6±0.6	7.5	-
356.5+02.2	PHR1728−3038	172807−303821	17 28 07.73	−30 38 21.3	3.3	4.6±0.5	16.9	-
356.6+02.3	PHR1728−3032	172814−303213	17 28 14.61	−30 32 13.2	5.4	2.3±0.5	9.8	-
355.8+01.7	MPA1728−3132	172831−313214	17 28 31.30	−31 32 14.6	6.2	14.4±1.3	4	12
355.6+01.4	PPA1729−3152	172911−315242	17 29 11.16	−31 52 42.6	3.2	8.2±0.6	5.5	-
008.3+09.6	PHR1729−1647	172912−164745	17 29 12.73	−16 47 45.7	9.0	2.4±0.5	20.5	-
352.8−00.5	MPA1729−3513	172937−351344	17 29 37.64	−35 13 44.1	2.6	72.8±2.3	12.7	-
000.4+04.4	PPA1729−2611	172952−261113	17 29 52.37	−26 11 13.6	0.7	11.1±0.6	9	1
000.3+04.2	PPA1730−2621	173012−262054	17 30 12.80	−26 20 54.5	9.3	3.0±0.5	6	1
358.4+02.7	PHR1731−2850	173114−285042	17 31 14.16	−28 50 42.6	5.9	3.5±0.6	17	-
003.1+05.2	PHR1733−2327	173307−232803	17 33 07.39	−23 28 03.2	4.6	3.4±0.5	13.4	-
002.5+04.8	PPA1733−2415	173322−241440	17 33 22.77	−24 14 40.8	24.2	4.6±0.5	16.9	-
000.3+03.4	PHR1733−2647	173327−264758	17 33 27.18	−26 47 58.6	1.1	3.8±0.6	14.5	-
357.9+01.7	PPA1733−2945	173338−294531	17 33 38.28	−29 45 31.1	1.9	4.2±0.5	7	-
358.4+02.1	PPA1733−2908	173340−290830	17 33 40.22	−29 08 30.4	5.1	2.7±0.5	9.5	-
357.8+01.6	PPA1734−2954	173401−295433	17 34 01.99	−29 54 33.6	4.0	12.8±0.6	13	-
006.2+06.9	PHR1734−2000				0.0	:2.0	19.5	-
350.9−02.9	PHR1734−3809	173420−380859	17 34 20.24	−38 08 59.4	7.2	7.8±1.3	61.1	-
352.7−01.7	PPA1734−3600	173422−360045	17 34 22.20	−36 00 45.0	3.2	8.0±0.6	9	-
358.0+01.6	PHR1734−2944	173429−294432	17 34 29.13	−29 44 32.3	3.7	2.4±0.5	13.5	-
358.6+02.0	PHR1734−2902	173429−290227	17 34 29.32	−29 02 27.1	23.2	16.1±2.8	53.1	1
356.9+00.9	PPA1734−3102	173434−310209	17 34 34.56	−31 02 09.6	3.7	12.5±0.6	5	-
357.7+01.4	PPA1734−3004				0.0	:2.0	7.7	-
359.4+02.3a	PPA1735−2809	173512−280933	17 35 12.30	−28 09 33.2	4.5	2.9±0.5	7.9	-
001.7+03.6	PHR1735−2527	173547−252739	17 35 47.34	−25 27 39.1	4.0	3.9±0.6	7	-
352.1−02.6	PHR1736−3659	173618−365950	17 36 18.89	−36 59 50.6	19.4	14.6±1.2	15.9	1
003.5+04.5	PHR1736−2330				0.0	:2.0	11.4	-
359.7+02.0	PPA1736−2804	173657−280441	17 36 57.09	−28 04 41.0	4.0	10.9±0.6	5.7	-
350.8−03.6	MPA1737−3837	173706−383721	17 37 06.13	−38 37 21.8	11.9	4.4±0.7	8	-
001.5+03.1	PHR1737−2559	173716−255933	17 37 16.35	−25 59 33.7	4.8	3.5±0.5	16.9	-
002.3+03.6	PPA1737−2501	173724−250137	17 37 24.12	−25 01 37.7	5.9	5.6±0.6	7	-
354.6−01.4	PPA1737−3414	173753−341424	17 37 53.82	−34 14 24.3	2.9	7.2±0.6	6	11
351.1−03.9	PHR1739−3829	173917−382929	17 39 17.20	−38 29 29.8	14.2	:11.2	45.3	1;27
354.5−02.0a	PPA1740−3437	174030−343713	17 40 30.17	−34 37 13.3	5.5	3.4±0.6	7	-
353.6−02.6	PPA1740−3543	174045−354359	17 40 45.94	−35 43 59.5	4.4	4.7±0.5	9	1
355.6−01.4	PHR1740−3324	174054−332418	17 40 54.75	−33 24 18.4	1.9	5.5±0.6	9	-
010.1+07.4	PHR1741−1624	174104−162450	17 41 04.87	−16 24 50.2	12.9	3.5±0.5	12.7	-
356.0−01.4	PPA1741−3302	174133−330208	17 41 33.52	−33 02 08.6	6.6	4.8±0.5	7.5	-

Table 5 – Continued

PNG	MASH Name	NVSS source	RAJ2000	DEJ2000	Offset [$''$]	S _{1.4GHz} [mJy]	θ_{opt} [$''$]	c.
355.2–02.0	PPA1741–3405	174159–340549	17 41 59.09	–34 05 49.7	15.7	3.5±0.6	6.5	1
356.0–01.8	PPA1743–3315	174307–331554	17 43 07.44	–33 15 54.9	3.1	5.8±0.5	5	-
003.5+02.6	PHR1743–2431	174338–243158	17 43 38.88	–24 31 58.2	7.7	4.3±0.6	30.4	-
352.2–04.3	PHR1743–3749	174348–375000	17 43 48.57	–37 50 00.0	12.1	2.6±0.6	35.5	-
356.5–01.8	PPA1744–3252	174427–325211	17 44 27.77	–32 52 11.8	3.0	6.1±0.6	6	13
356.6–01.9	PHR1745–3246	174509–324616	17 45 09.55	–32 46 16.5	3.2	30.3±1.6	43.2	1;18
353.8–03.7	PHR1745–3609	174531–361011	17 45 31.56	–36 10 11.3	16.3	3.0±0.6	30.4	1
356.1–02.7	PPA1747–3341	174705–334112	17 47 05.46	–33 41 12.0	12.2	4.7±0.8	5.2	1
007.8+04.3	PHR1747–1957	174715–195723	17 47 15.74	–19 57 23.3	5.8	2.3±0.5	15.9	-
002.0+00.7	MPA1747–2649	174728–264948	17 47 28.15	–26 49 48.1	2.0	4.1±0.5	4	-
357.3–02.0	PPA1747–3215	174728–321546	17 47 28.46	–32 15 46.0	0.5	4.2±0.5	4.5	-
354.5–03.9	PHR1748–3538	174815–353846	17 48 15.79	–35 38 46.4	16.6	3.2	46.7	1;28
004.3+01.8a	PHR1748–2417	174832–241738	17 48 32.87	–24 17 38.7	3.2	3.8±0.6	13.5	-
003.5+01.3	MPA1748–2511	174841–251135	17 48 41.74	–25 11 35.8	1.9	24.9±0.9	4.5	-
005.0+02.2	PHR1748–2326	174845–232627	17 48 45.10	–23 26 27.2	12.4	3.7±0.6	10.2	-
357.5–02.4	PPA1749–3216	174938–321630	17 49 38.05	–32 16 30.4	3.1	7.3±0.5	8.4	-
009.9+04.5	PHR1750–1803	175047–180334	17 50 47.62	–18 03 34.0	4.0	4.9±0.6	26.2	-
358.0–02.4	PPA1750–3152	175048–315224	17 50 48.27	–31 52 24.7	3.7	4.6±0.6	6	-
000.0–01.3	PPA1751–2933	175059–293347	17 50 59.46	–29 33 47.7	12.7	4.5±0.8	11	2
008.8+03.8	PHR1751–1925	175107–192540	17 51 07.74	–19 25 40.8	14.9	3.0±0.5	10	-
010.0+04.3	PHR1751–1804	175144–180425	17 51 44.84	–18 04 25.5	28.9	3.8	27.5	1
003.7+00.5	PHR1752–2527	175208–252746	17 52 08.55	–25 27 46.8	1.4	23.1±1.2	11.7	1
000.1–01.7	PHR1752–2941	175248–294205	17 52 48.74	–29 42 05.7	7.0	2.9±0.6	13.9	-
000.3–01.6	PHR1752–2930	175252–293000	17 52 52.19	–29 30 00.6	1.2	4.1±0.5	8	14
001.1–01.2	PPA1753–2836	175317–283602	17 53 17.42	–28 36 02.9	3.1	8.8±0.6	10.7	-
355.9–04.4	PHR1753–3443	175339–344340	17 53 39.83	–34 43 40.2	5.9	15.0±0.7	20.1	-
006.1+01.5	PHR1753–2254	175345–225402	17 53 45.35	–22 54 02.5	1.6	25.2±1.2	20.6	-
357.8–03.3	PHR1753–3228	175354–322847	17 53 54.92	–32 28 47.6	13.9	3.1±0.5	32	-
002.1–01.1	MPA1755–2741	175510–274131	17 55 10.19	–27 41 31.9	8.6	2.7±0.5	8	-
007.3+01.7	PHR1755–2142	175535–214244	17 55 35.07	–21 42 44.8	8.5	5.0±0.6	16	-
006.9+01.5	MPA1755–2212	175536–221256	17 55 36.72	–22 12 56.8	9.8	4.0±0.5	4	-
007.4+01.7	PHR1755–2140	175542–214017	17 55 42.82	–21 40 17.8	3.1	3.1±0.5	16.7	-
001.0–01.9	PHR1755–2904	175543–290408	17 55 43.07	–29 04 08.0	3.0	4.8±0.6	13.5	-
002.2–01.2	PPA1755–2739	175545–273942	17 55 45.36	–27 39 42.9	3.7	8.0±0.5	12.6	-
013.1+05.0	PHR1755–1502	175546–150247	17 55 46.48	–15 02 47.8	4.0	3.7±0.5	17.1	-
012.5+04.3	PHR1757–1556	175710–155620	17 57 10.61	–15 56 20.5	3.0	3.7±0.7	26.9	-
011.8+03.7	PHR1757–1649	175740–164915	17 57 40.72	–16 49 15.9	16.4	14.5±1.8	137.7	1
010.2+02.7	PHR1758–1841	175814–184125	17 58 14.40	–18 41 25.2	0.8	18.3±0.7	8	1
357.8–04.4	PHR1758–3304	175826–330501	17 58 26.50	–33 05 01.6	8.0	2.4±0.5	17.7	-
007.8+01.2	MPA1758–2135	175833–213519	17 58 33.95	–21 35 19.6	4.6	8.8±0.6	5	-
003.5–01.2	PPA1758–2628	175837–262848	17 58 37.05	–26 28 48.9	2.0	13.7±0.6	4.5	-
008.1+01.3	PHR1758–2112	175840–211240	17 58 40.66	–21 12 40.4	5.7	6.1±0.6	9.9	-
010.2+02.4	PHR1759–1853	175905–185337	17 59 05.49	–18 53 37.3	16.3	2.9±0.7	10.8	-
003.6–01.3	PHR1759–2630	175912–263026	17 59 12.11	–26 30 26.8	2.8	47.7±1.5	8.5	1
003.1–01.6	PHR1759–2706	175926–270623	17 59 26.08	–27 06 23.7	10.3	3.7±0.6	33.8	-
003.0–01.7	PHR1759–2712	175932–271245	17 59 32.85	–27 12 45.1	6.8	5.0±0.7	65.2	-
003.3–01.6	PHR1759–2651	175955–265131	17 59 55.19	–26 51 31.8	17.3	4.2±0.6	8.8	1
001.7–02.6	PPA1800–2846	180001–284628	18 00 01.27	–28 46 28.8	9.0	2.5±0.5	14.6	-
010.6+02.4	MPA1800–1834	180008–183436	18 00 08.49	–18 34 36.3	4.7	6.3±0.6	9	-
003.4–01.8	PHR1800–2653	180042–265334	18 00 42.26	–26 53 34.6	2.5	4.7±0.5	11.5	-
004.8–01.1	PHR1801–2522	180116–252239	18 01 16.90	–25 22 39.6	1.6	67.3±2.5	8.4	3
004.3–01.4	PPA1801–2553	180118–255323	18 01 18.92	–25 53 23.2	2.2	12.7±0.7	5.5	-
014.7+04.3	MPA1801–1402	180146–140205	18 01 46.34	–14 02 05.2	14.0	2.5±0.6	5	-
003.8–01.9	PHR1802–2637	180210–263700	18 02 10.68	–26 37 00.6	10.2	2.7±0.6	8.2	-
012.4+02.4	MPA1803–1657	180355–165724	18 03 55.07	–16 57 24.2	2.2	21.5±0.8	11	-
012.9+02.6	MPA1804–1627	180410–162743	18 04 10.45	–16 27 43.7	0.8	5.6±0.5	10	-
011.0+01.4	PHR1804–1842	180428–184241	18 04 28.62	–18 42 41.5	8.3	14.1±0.7	17.5	-
004.2–02.5	PHR1805–2631	180519–263146	18 05 19.34	–26 31 46.9	10.4	4.6±0.6	9.7	-
004.1–03.3	PPA1808–2700	180800–270017	18 08 00.78	–27 00 17.4	8.4	3.6±0.7	11.4	-
015.5+02.8	BMP1808–1406	180825–140912	18 08 25.91	–14 09 12.9	200.0	3.8	470	29
016.6+03.1	PHR1809–1300	180935–130007	18 09 35.34	–13 00 07.6	15.8	6.0±0.7	14.4	-
013.3+01.1	PHR1810–1647	181011–164724	18 10 11.64	–16 47 24.1	37.6	>5.3	121	1;19
009.4–01.2	PHR1811–2123	181110–212312	18 11 10.78	–21 23 12.7	2.8	18.6±0.8	16.2	-
009.8–01.1	PHR1811–2100	181139–210043	18 11 39.20	–21 00 43.6	2.8	3.3±0.6	19.6	-
007.5–02.4	PPA1811–2337	181140–233717	18 11 40.65	–23 37 17.9	2.0	9.2±0.6	9.9	-
008.6–02.2	PPA1813–2233	181311–223322	18 13 11.19	–22 33 22.7	9.2	3.2±0.7	7.2	-
006.4–03.4	PHR1813–2505	181326–250538	18 13 26.82	–25 05 38.8	13.4	3.7±0.8	26.5	-
014.6+01.0	PHR1813–1543	181330–154358	18 13 30.06	–15 43 58.7	42.5	8.5	23.8	1
017.6+02.6	PHR1813–1220	181333–122047	18 13 33.69	–12 20 47.8	0.2	26.6±0.9	8	-
010.0–01.5	PHR1813–2057	181335–205705	18 13 35.35	–20 57 05.3	0.8	33.4±1.1	13.4	4
015.5+01.0	PHR1815–1457	181506–145723	18 15 06.61	–14 57 23.1	2.6	9.2±0.6	8.5	-
008.4–02.8	PHR1815–2300	181513–230105	18 15 13.07	–23 01 05.2	1.5	3.2±0.6	13	-
014.5+00.4	MPA1815–1602	181521–160259	18 15 21.19	–16 02 59.7	3.9	10.5±0.6	5.5	-
010.0–02.0	MPA1815–2113	181537–211318	18 15 37.26	–21 13 18.0	4.7	19.0±0.8	8	-
010.7–02.3	MPA1818–2044	181804–204411	18 18 04.44	–20 44 11.8	2.3	5.7±0.5	10.8	-

Table 5 – Continued

PNG	MASH Name	NVSS source	RAJ2000	DEJ2000	Offset [$''$]	S _{1.4GHz} [mJy]	θ_{opt} [$''$]	c.
017.5+01.0	MPA1819–1307	181903–130717	18 19 03.37	–13 07 17.2	20.5	:5.2	5.5	-
020.4+02.2	PHR1820–1002	182015–100228	18 20 15.28	–10 02 28.9	1.8	4.9±0.7	21.1	-
012.1–02.1	PHR1820–1926	182017–192637	18 20 17.95	–19 26 37.1	6.4	4.4±0.5	10.2	-
020.4+02.0	MPA1820–1009	182050–100945	18 20 50.75	–10 09 45.9	3.6	3.3±0.7	6	-
011.0–02.9	PHR1820–2048	182053–204813	18 20 53.71	–20 48 13.6	2.0	15.0±1.1	14.9	1
012.1–02.5	PHR1821–1939	182143–193944	18 21 43.32	–19 39 44.5	7.6	2.5±0.5	12.2	-
021.3+02.2	MPA1822–0914	182206–091401	18 22 06.14	–09 14 01.0	10.3	4.3±0.8	8	-
027.7+05.1	PHR1823–0214	182347–021433	18 23 47.85	–02 14 33.3	5.3	2.6±0.6	28.1	-
013.4–02.9	PHR1825–1839	182535–183942	18 25 35.63	–18 39 42.8	2.2	4.9±0.6	29.2	-
025.9+03.4	PHR1826–0435	182617–043525	18 26 17.94	–04 35 25.6	5.7	18.5±1.3	17.5	5
021.2+00.9	PHR1826–0953	182626–095327	18 26 26.55	–09 53 27.5	6.8	8.4±0.6	47.6	-
022.0+01.3	PHR1826–0859	182627–085915	18 26 27.90	–08 59 15.1	7.7	4.5±0.6	44	1
018.2–00.9	MPA1827–1328	182729–132819	18 27 29.74	–13 28 19.1	1.2	34.5±1.2	12	-
016.8–01.7	BMP1827–1504	182750–150425	18 27 50.72	–15 04 25.4	1.8	11.6±0.7	8	-
025.6+02.8	MPA1827–0510	182757–051019	18 27 57.24	–05 10 19.3	4.4	4.7±0.5	10	-
024.2+01.8	MPA1828–0652	182847–065159	18 28 47.85	–06 51 59.9	2.2	3.5±0.5	7	-
026.4+02.7	PHR1829–0431	182934–043135	18 29 34.15	–04 31 35.5	2.6	10.2±0.5	18.2	6
018.5–01.6	PHR1830–1331	183042–133111	18 30 42.31	–13 31 11.8	3.1	5.9±0.6	18.4	-
024.1+01.1	PHR1831–0715	183116–071525	18 31 16.87	–07 15 25.1	4.0	5.9±0.5	16.9	-
018.0–02.2	PHR1831–1415	183151–141519	18 31 51.05	–14 15 19.6	11.5	10.9±1.5	56.9	-
019.2–01.6	MPA1831–1256	183152–125613	18 31 52.98	–12 56 13.7	0.4	15.0±0.7	11	-
018.7–01.8	PHR1832–1326	183204–132616	18 32 04.70	–13 26 16.3	8.8	5.9±0.6	38.9	-
024.4+00.9	MPA1832–0706	183222–070648	18 32 22.93	–07 06 48.0	9.0	5.5±0.5	14	-
027.8+02.7	PHR1832–0317	183231–031743	18 32 31.50	–03 17 43.1	3.5	11.3±1.4	19.7	-
027.0+01.5	PHR1835–0429	183511–042903	18 35 11.68	–04 29 03.1	3.1	62.0±2.7	39.5	-
027.0+01.3	MPA1835–0440	183553–044009	18 35 53.71	–04 40 09.0	1.7	9.5±0.6	7	-
029.0+02.2	MPA1836–0227	183610–022710	18 36 10.77	–02 27 10.8	3.4	12.2±0.6	10	-
032.5+03.2	MPA1839+0106	183911+010617	18 39 11.80	+01 06 17.9	7.1	6.1±0.6	10	-
022.8–01.9	MPA1839–0953	183944–095313	18 39 44.48	–09 53 13.7	3.5	5.1±0.5	9.4	-
030.2+01.5	MPA1841–0140	184104–014044	18 41 04.41	–01 40 44.1	5.1	4.4±0.7	8.9	-
032.6+02.4	MPA1842+0050	184211+005032	18 42 11.43	+00 50 32.8	0.9	15.1±0.7	6	-
023.2–02.6	MPA1842–0949	184257–094956	18 42 57.28	–09 49 56.5	9.0	11.1±0.7	9	-
032.0+01.7	PHR1843+0002	184345+000222	18 43 45.06	+00 02 22.2	1.3	10.7±0.6	13	-
029.8+00.5	PHR1843–0232	184358–023155	18 43 58.05	–02 31 55.4	21.3	:33	57.4	1
026.8–01.0	MPA1843–0556	184358–055626	18 43 58.76	–05 56 26.2	14.2	5.5±0.9	11.4	-
026.7–01.2	PHR1844–0603	184428–060326	18 44 28.82	–06 03 26.8	3.2	2.6±0.5	14	-
027.6–00.8	PHR1844–0503	184445–050421	18 44 45.91	–05 04 21.7	27.9	:3.2	20.5	1
032.5+01.5	PHR1845+0021	184500+002116	18 45 00.37	+00 21 16.4	8.2	3.6±0.5	30.9	-
033.8+01.5	PHR1847+0132	184745+013248	18 47 45.45	+01 32 48.1	1.3	13.4±0.6	43.4	-
016.0–07.6	PHR1848–1829	184811–182927	18 48 11.46	–18 29 27.4	15.8	3.0±0.6	18.8	-
024.4–03.5	PHR1848–0912	184832–091156	18 48 32.56	–09 11 56.6	5.8	6.0±0.7	16.9	-
028.5–01.4	PHR1848–0435	184842–043605	18 48 42.02	–04 36 05.6	21.2	5.6±0.7	43	1
026.2–03.4	PHR1851–0732	185131–073238	18 51 31.17	–07 32 38.1	9.3	6.2±0.5	39.7	-
032.5–00.4	MPA1852–0033	185225–003323	18 52 25.45	–00 33 23.0	3.1	20.5±0.8	9	-
031.1–01.3	MPA1852–0210	185255–021057	18 52 55.87	–02 10 57.5	1.8	11.7±0.6	7.5	-
031.0–02.1	MPA1855–0240	185534–024022	18 55 34.56	–02 40 22.6	4.4	8.7±0.5	7.5	-
035.5–00.4	PHR1857+0207	185759+020708	18 57 59.75	+02 07 08.8	4.2	100±4	11	1
034.1–01.6	MPA1859+0017	185925+001739	18 59 25.02	+00 17 39.0	12.4	3.7±0.6	8.9	7
033.7–02.0a	PHR1900–0014	190003–001356	19 00 03.94	–00 13 56.4	14.7	2.5±0.5	41	-
034.0–02.2	MPA1901+0000	190136+000012	19 01 36.01	+00 00 12.8	1.8	2.5±0.5	7	-
035.6–04.2	MPA1911+0027	191125+002756	19 11 25.57	+00 27 56.1	16.0	3.4±0.6	26.9	-

Table 6. MASH PNe positively detected in the MPGS-2.

PNG	MASH Name	MGPS2 source	RAJ2000	DEJ2000	Offset [$''$]	S _{0.843GHz} [mJy]	θ_{opt} [$''$]	c.
248.3–03.6	PHR0748–3258	J074831–325823	07 48 31.96	–32 58 23.6	7.8	18.0±1.7	22.5	-
250.5–03.4	PHR0754–3444	J075455–344407	07 54 55.60	–34 44 07.3	2.1	24.7±2.3	59.5	-
274.2–09.7	FP0840–5754	J084023–575501	08 40 23.81	–57 55 01.4	14.0	21.9±1.1	339.9	-
269.3–00.8	PHR0905–4822	J090528–482251	09 05 28.79	–48 22 51.3	6.1	16.2±2.2	23.1	-
292.4–00.7	MPA1121–6146	J112121–614608	11 21 21.73	–61 46 08.1	2.1	40.3±2.6	6.5	-
294.7–02.4	MPA1135–6406	J113546–640618	11 35 46.43	–64 06 18.6	0.4	20.0±1.3	11	-
297.0–04.9	PHR1150–6704	J115028–670519	11 50 28.49	–67 05 19.6	23.2	14.6±1.8	45.4	23
302.3–00.5	PHR1246–6324	J124627–632431	12 46 27.54	–63 24 31.3	7.7	17.8±2.1	24.3	15
309.8–01.6	MPA1354–6337	J135421–633714	13 54 21.99	–63 37 14.5	4.1	13.7±1.2	7.5	-
310.8–02.3	MPA1404–6403	J140424–640402	14 04 24.31	–64 04 02.2	8.8	13.5±1.7	6	-
314.4+01.3	BMP1423–5923	J142359–592337	14 23 59.57	–59 23 37.3	1.2	14.8±1.4	8.5	-
315.9+00.3	PHR1437–5949	J143753–594917	14 37 53.09	–59 49 17.7	7.3	18.4±2.8	80.6	-
316.9+01.8	MPA1440–5802	J144027–580219	14 40 27.00	–58 02 19.7	3.3	11.8±1.0	11.5	-
315.7–01.1	MPA1441–6114	J144132–611417	14 41 32.71	–61 14 17.6	3.7	20.3±1.7	6.5	-
318.9+00.7	PHR1457–5812	J145735–581205	14 57 35.66	–58 12 05.4	3.6	83.3±2.9	27.8	-
319.5–01.0	PHR1507–5925	J150750–592514	15 07 50.63	–59 25 14.0	3.3	24.2±1.5	19.3	-
321.3–00.3	PHR1517–5751	J151731–575110	15 17 31.35	–57 51 10.7	1.4	65.1±7.7	104.2	-
322.2–00.4	BMP1522–5729	J152258–573000	15 22 58.68	–57 30 00.7	2.5	17.2±1.5	12	-
322.2–00.7	BMP1524–5746	J152423–574621	15 24 23.85	–57 46 21.9	1.5	27.0±1.8	7	-
323.5+01.1	MPA1525–5528	J152506–552827	15 25 06.25	–55 28 27.7	5.8	22.8±1.4	13.8	-
322.0–01.3	BMP1525–5823	J152559–582303	15 25 59.37	–58 23 03.7	1.7	27.2±2.2	8.9	-
322.0–01.8	PHR1527–5846	J152735–584616	15 27 35.88	–58 46 16.8	6.0	15.4±1.5	16.3	-
324.3+01.1	PHR1529–5458	J152927–545914	15 29 27.96	–54 59 14.3	22.7	37.1±4.6	92.5	25
322.7–01.4	MPA1530–5801	J153050–580125	15 30 50.50	–58 01 25.5	4.7	16.9±1.7	6	-
327.1+01.9	MPA1541–5243	J154129–524350	15 41 29.41	–52 43 50.9	2.1	39.1±1.9	11	-
332.3+07.0	PHR1547–4533	J154743–453243	15 47 43.94	–45 32 43.4	17.8	27.7	118.9	26
328.3+00.7	PHR1552–5254	J155257–525408	15 52 57.28	–52 54 08.5	5.6	20.9±2.3	28.4	-
334.4+02.3	BMP1614–4742	J161451–474211	16 14 51.82	–47 42 11.1	4.8	12.3±1.3	11.5	-
333.9+00.6	PHR1619–4914	J161940–491358	16 19 40.18	–49 13 58.4	1.8	294.8±9.7	33.9	-
338.9+04.6	PHR1624–4252	J162400–425239	16 24 00.27	–42 52 39.8	6.5	10.3±1.6	40	-
340.4+03.8	MPA1632–4220	J163231–422053	16 32 31.40	–42 20 53.9	3.3	20.6±1.2	14.4	-
337.3+00.6	PHR1633–4650	J163358–465009	16 33 58.18	–46 50 09.0	2.7	47.2±5.5	13.9	-
340.0+02.9	PHR1634–4318	J163442–431759	16 34 42.81	–43 17 59.5	3.2	14.6±1.1	16.4	-
338.6+01.1	BMP1636–4529	J163658–452935	16 36 58.20	–45 29 35.9	8.7	22.0±4.2	9.9	-
335.4–01.9	PHR1637–4957	J163744–495747	16 37 44.86	–49 57 47.3	2.7	37.0±1.9	19.2	-
338.4–02.0	MPA1650–4747	J165009–474705	16 50 09.87	–47 47 05.1	0.7	14.6±1.6	5	-
343.5+01.2	PHR1653–4143	J165355–414357	16 53 55.50	–41 43 57.9	3.1	18.7±1.9	12.8	-
340.1–02.2a	MPA1657–4633	J165706–463357	16 57 06.27	–46 33 57.2	2.8	12.6±1.6	7	-
341.9–02.8	MPA1706–4527	J170624–452659	17 06 24.71	–45 26 59.0	7.2	22.2±3.5	7.5	-
350.4+02.0	PHR1712–3543	J171233–354321	17 12 33.85	–35 43 21.5	2.4	12.7±1.9	10.1	-
347.2–00.8	PHR1714–4006	J171447–400600	17 14 47.77	–40 06 00.0	19.7	25.6±6.8	14.8	-
344.8–02.6	MPA1715–4303	J171515–430357	17 15 15.59	–43 03 57.6	5.0	17.6±2.2	7	-
353.6+01.7	PPA1722–3317	J172235–331704	17 22 35.43	–33 17 04.4	10.6	18.6±2.9	4	-
355.0+02.6	PPA1722–3139	J172240–313954	17 22 40.68	–31 39 54.9	1.5	19.1±2.7	8.5	-
354.8+01.8	PPA1725–3216	J172515–321607	17 25 15.81	–32 16 07.6	3.6	17.6±3.4	6.9	-
355.6+01.4	PPA1729–3152	J172911–315243	17 29 11.04	–31 52 43.0	2.1	11.6±2.1	5.5	-
352.8–00.5	MPA1729–3513	J172937–351339	17 29 37.20	–35 13 39.8	7.2	56±5	12.7	-
357.8+01.6	PPA1734–2954	J173401–295442	17 34 01.96	–29 54 42.9	8.6	13.8±1.8	13	-
352.1–02.6	PHR1736–3659	J173617–365937	17 36 17.86	–36 59 37.2	11.9	15.4±2.4	15.9	-
356.6–01.9	PHR1745–3246	J174509–324629	17 45 09.46	–32 46 29.2	12.9	33.7±2.8	43.2	18
355.9–04.4	PHR1753–3443	J175339–344336	17 53 39.87	–34 43 36.2	7.2	20.9±1.8	20.1	-
001.0–01.9	PHR1755–2904	J175543–290406	17 55 43.23	–29 04 06.8	2.5	15.5±2.3	13.5	-
003.6–01.3	PHR1759–2630	J175912–263033	17 59 12.00	–26 30 33.4	9.5	32.7±3.0	8.5	-

Table 7. MASH PNe possibly detected in the MPGS-2.

PNG	MASH Name	J2000 des.	RAJ2000	DEJ2000	Offset [']	S _{0.843GHz} [mJy]	θ_{opt} ['']	c.
272.8+01.0	PHR0928-4936	J0928-4936	09 28 41.79	-49 36 54.4	20.7	7.5	85.5	-
291.6-00.2	PHR1115-6059	J1115-6059	11 15 48.16	-60 59 13.4	25.0	>18.7	102.5	16
297.0+01.1	PHR1202-6112	J1202-6112	12 02 17.02	-61 12 45.6	14.8	7.3	13.5	-
299.2+01.0	PHR1220-6134	J1220-6134	12 20 09.21	-61 34 20.3	7.5	7.4	9.7	-
301.5+02.0	MPA1239-6048	J1239-6048	12 39 46.20	-60 48 15.9	1.9	7.5	6.9	-
304.8-01.4	MPA1309-6415	J1309-6415	13 09 30.16	-64 15 31.9	11.1	5.7	8.9	-
305.6-00.9	MPA1315-6338	J1315-6338	13 15 30.89	-63 38 37.7	9.1	9.8	6	-
305.9-01.6	MPA1319-6418	J1319-6419	13 19 24.47	-64 19 05.7	14.5	6.7	4	-
309.5+00.8	PHR1346-6116	J1346-6116	13 46 39.37	-61 16 14.2	21.7	6.8	61	24
313.4+06.2	MPA1405-5507	J1405-5507	14 05 31.49	-55 07 42.3	7.8	6.0	8	-
313.9+01.4	PHR1420-5933	J1420-5933	14 20 07.09	-59 33 48.1	10.6	7.7	28.9	-
315.2-01.3	PHR1438-6140	J1438-6140	14 38 18.03	-61 40 07.2	5.3	5.6	27	-
318.2-02.3	PHR1504-6113	J1504-6113	15 04 39.97	-61 13 06.8	7.0	9.0	15.9	-
322.7+02.6	PHR1514-5436	J1514-5436	15 14 34.42	-54 36 08.6	6.2	6.6	21.8	-
322.4-00.1a	MPA1523-5710	J1523-5710	15 23 22.09	-57 10 54.0	6.1	18.3	14.5	8
325.7+02.2	BMP1533-5319	J1533-5319	15 33 20.29	-53 19 03.7	5.4	8.7	17.2	-
324.1-01.3	MPA1539-5709	J1539-5709	15 39 10.56	-57 09 56.6	5.6	9.8	9.4	-
331.3+01.6	PHR1603-5016	J1603-5017	16 03 54.01	-50 17 01.4	10.5	7.6	14.9	-
329.5-00.8	MPA1605-5319	J1605-5320	16 05 36.95	-53 20 03.7	11.8	11.7	6.9	-
332.3-00.9	PHR1619-5131	J1619-5131	16 19 58.85	-51 31 48.2	20.3	13.7	11	9
331.8-02.3	MPA1624-5250	J1624-5250	16 24 03.72	-52 50 17.6	16.9	>7.2	9	-
337.4+02.6	PHR1625-4522	J1625-4521	16 25 51.21	-45 21 22.3	76.8	>11.1	314.6	17
344.4-03.5	MPA1717-4351	J1717-4351	17 17 52.90	-43 51 52.9	6.8	8.3	7	-
354.7+03.2	PHR1719-3134	J1719-3134	17 19 54.55	-31 34 32.5	15.8	14.8	6.7	-
354.4+02.2	PPA1723-3223	J1723-3222	17 23 04.00	-32 22 52.8	17.5	10.7	9.4	-
355.8+01.7	MPA1728-3132	J1728-3132	17 28 30.87	-31 32 13.2	5.4	10.2	4	-
356.1-02.1	PHR1744-3319	J1744-3319	17 44 51.04	-33 19 32.6	11.7	9.6	8.5	-
359.4-05.6	BMP1807-3215	J1807-3215	18 07 05.77	-32 15 12.2	20.9	7.9	20.4	-

APPENDIX A: FINDING CHARTS AND SELECTED NOTES ON INDIVIDUAL MASH PNE

In this appendix we present the MASH PNe finding charts used in this study (radio contour images and optical SHS *quotient* images overlaid with radio contours). The SHS *quotient* images were constructed as SHS H α divided by SHS short red image. This technique allows better examination of spatial properties of extended and low surface brightness PNe (for more details see Miszalski et al. 2008). In Fig. A1 we present nine MASH PNe detected in the PMN survey. Furthermore, we give more detailed descriptions of some of the positively or possibly identified radio counterparts of MASH PNe in the NVSS and MGPS-2. We discuss MASH PNe radio detections with nearby and bright radio objects which could be the source of a confusion and/or radio detections for which we found some discrepancy in the association with the optical emission. Detailed descriptions of individual identifications for PNe with comment key 1 were given in LCY05. Corresponding radio-continuum contour images, if available, are presented in Figures A2 and A3. In Figures A4 and A5 we present SHS *quotient* images overlaid with radio contours of several positive and suspect radio detected MASH PNe. All objects from this set have optical angular diameters comparable or larger than the resolution of a corresponding radio image. Finally, the radio contour plots of 25 possibly detected MASH PNe radio counterparts from the MGPS-2 survey, not catalogued in the MGPS-2 catalogue, are presented in Fig. A6 and Fig. A7.

(2) G000.0-01.3 (PPA1751-2933; Fig. A2): Faint, oval nebula, designated as “likely” PN. The optical angular diameter is ~ 12 arcsec while the faint radio source appears to be more extended.

(3) G004.8-01.1 (PHR1801-2522; Fig. A2): Confirmed, compact PN, very bright at 1.4 GHz (~ 67 mJy). Faint wings are very likely image artefacts and not associated with the nebula.

(4) G010.0-01.5 (PHR1813-2057; Fig. A2): Confirmed, bright, oval and compact PN with possible ansae and MSX detection in all 4 bands. The faint radio extension to the south (~ 4 mJy) is very likely not associated with the nebula.

(5) G025.9+03.4 (PHR1826-0435; Fig. A2): Faint, slightly oval, true PN with enhanced opposing lobes and bipolar core. Optical angular diameter (~ 20 arcsec) is a factor of two smaller than FWHM of the NVSS restoring beam. Thus, the radio “wing” is probably a background source.

(6) G026.4+02.7 (PHR1829-0431; Fig. A2): Small (~ 20 arcsec), faint, semi-circular nebula with bipolar core designated as a true PN. The radio “wing”, extending to the south of the nebula, is not visible in available optical bands and it is very likely a faint background source.

(7) G034.1-01.6 (MPA1859+0017; Fig. A2): Faint and compact (~ 10 arcsec) confirmed PN. Radio source, located ~ 90 arcsec from the radio detection, appears slightly extended but not correlated to this PN.

(8) G322.4-00.1a (MPA1523-5710; Fig. A2): Confirmed bipolar PN from the MASH-II supplement super-imposed over the shell of the nearby SNR G322.5-00.1 discovered in the MOST survey of the southern Galactic plane (Whiteoak 1992).

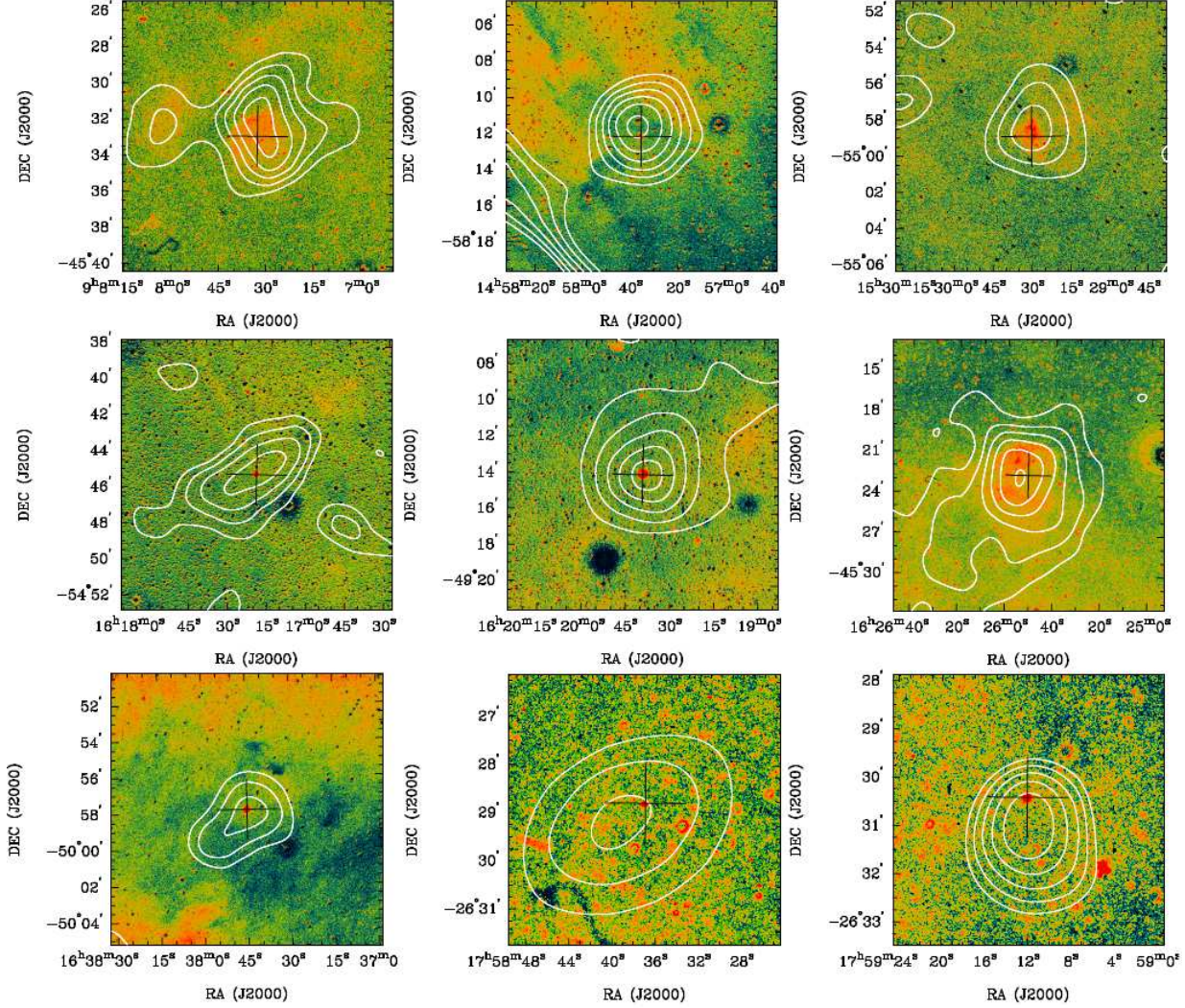


Figure A1. Finding charts of MASH PNe with PMN radio counterparts. Finding charts are produced as radio-continuum contour maps from the PMN superposed on the SHS *quotient* images (see text for more details). **First row from left to right:** PHR0907-4532, contours are at 20, 30, 40, 60 and 50 mJy; PHR1457-5812, contours are at 20, 30, 40, 50, 60 and 70 mJy and PHR1529-5458, contours are at 20, 30 and 40 mJy. **Second row from left to right:** PHR1617-5445, contours are at 20, 25, 30 and 35 mJy; PHR1619-4914, contours are at 20, 60, 100, 140 and 180 mJy and PHR1625-4522, contours are at 20, 40, 60, 80, 100 and 120 mJy. **Third row from left to right:** PHR1637-4957, contours are at 20, 30 and 40 mJy; PPA1758-2628, contours are at 40, 50 and 60 mJy and PHR1759-2630, contours are at 40, 42, 44, 46 and 48 mJy.

The southern radio extension is a part of the SNR shell and it is not correlated to this PN. However, the fitted flux could be overestimated as a result of the underlying large scale structure.

(9) G332.3-00.9 (PHR1619-5131; Fig. A2): While the coincidence of the optical position from the MASH with the radio excess in the SUMSS/MGPS-2 radio image looks quite convincing we didn't find a radio counterpart in the MGPS-2 catalogue. Thus, this PN is designated with suspect radio identification. The measured flux density of 13.7 mJy is well above the usual *rms* noise of 1.0 mJy Beam⁻¹. However, the local *rms* noise (or the large scale structures) in the vicinity of this PN is significantly above the average (~ 4 mJy Beam⁻¹).

(10) G352.6+02.2 (PPA1717-3349; Fig. A3): A compact optical nebula ($\theta_{opt} < 10$ arcsec), designated as a “likely” PN. The nearby extended radio source has a positional association with the IRAS source 17146-3344. The ratio between IRAS fluxes at 12 μ m and 25 μ m is 1.3, which implies association with an OH/IR star. The extended source is relatively faint ($S_{1.4\text{GHz}} < 15$ mJy) so the confusion of this PN is probably only a mild one.

(11) G354.6-01.4 (PPA1737-3414; Fig. A3): The radio flux (~ 7 mJy) from the compact ($\theta_{opt} \approx 6$ arcsec) true PN, is probably highly confused from the much brighter, and very likely unrelated, nearby object ($S_{1.4\text{GHz}} = 177$ mJy).

(12) G355.8+01.7 (MPA1728-3132; Fig. A3): Confirmed planetary nebula from the MASH-II supplement. Optical size of the nebula is 4 arcsec. The position of the correlated NVSS radio peak is ~ 6 arcsec away from the estimated optical position.

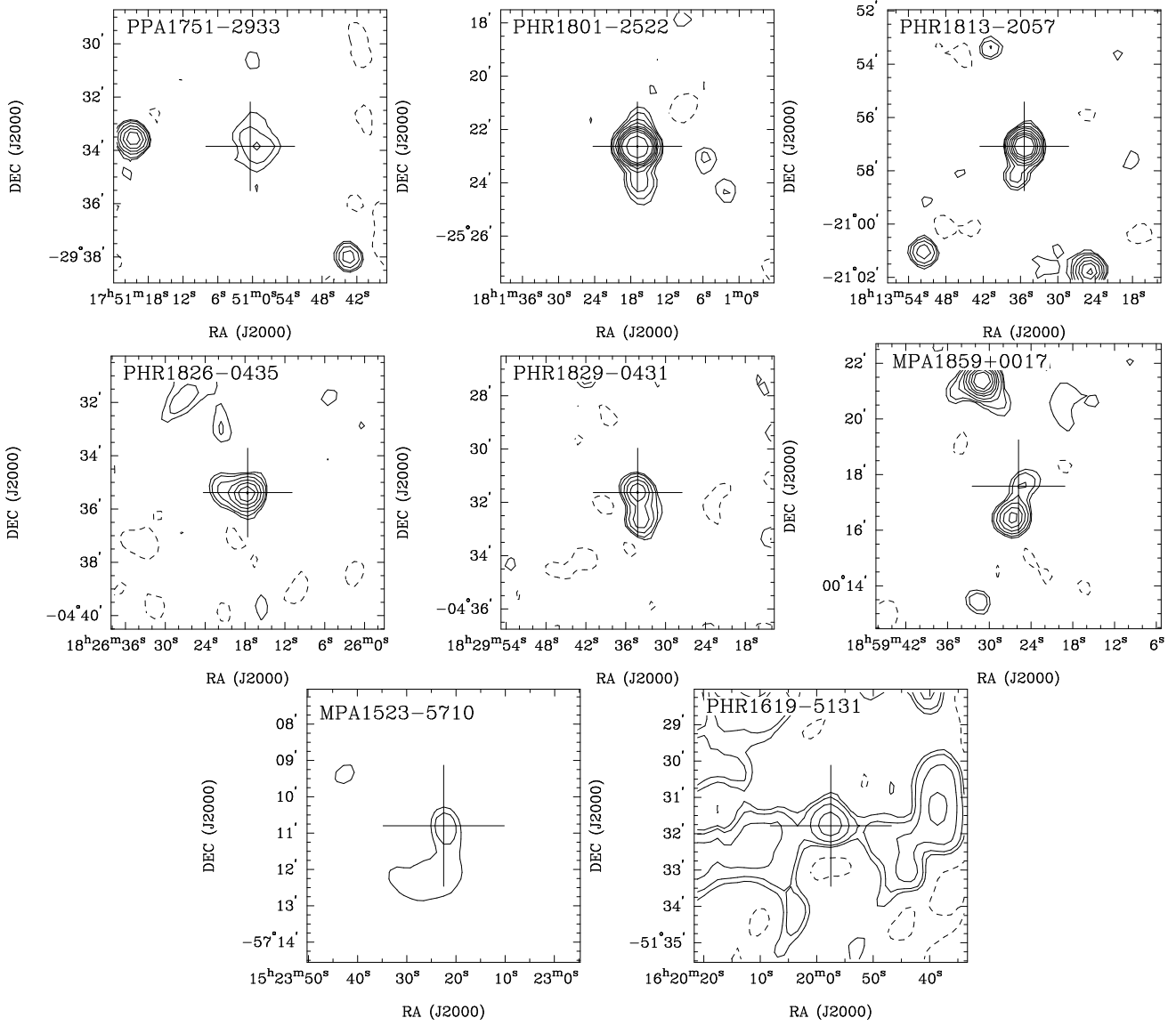


Figure A2. Radio-continuum contour plots of MASH PNe detected or possibly detected in the NVSS/MGPS-2. First row (from left to right): PPA1751–2933 (NVSS), PHR1801–2522 (NVSS) and PHR1813–2057 (NVSS). Second row (from left to right): PHR1826–0435 (NVSS), PHR1829–0431 (NVSS) and MPA1859+0017 (NVSS). Third row (from left to right): MPA1523–5710 (MGPS-2) and PHR1619–5131 (MGPS-2). Contours are at $-2, 2, 3, 5, 8, 12, 17, 23, 30, 60$ and $120 \times \sigma_{rms}$ (where σ_{rms} is a local rms noise). Negative contour (at $-2 \times \sigma_{rms}$) is presented with a dashed line. Radio-continuum contour images are overlaid with a cross centred in the MASH PN optical position. MASH PN designation is in the upper left corner.

Also, the radio source appears to be relatively extended. This implies that the angular size of this PN could be much larger than seen in $H\alpha$.

(13) G356.5–01.8 (PPA1744–3252; Fig. A3): Possible PN. The radio-continuum flux (~ 6 mJy) from the compact ($\theta_{opt} \approx 6$ arcsec) nebula, is probably only mildly confused from the nearby, stronger, radio source (174423–325116; $S_{1.4\text{GHz}} = 31$ mJy).

(14) G000.3-01.6 (PHR1752–2930; Fig. A3): Compact ($\theta_{opt} \approx 8$ arcsec), true PN close to star. Radio detected by Van de Steene & Jacoby (2001) with measured flux densities at 6 cm and 3 cm of 8.5 mJy and 2.5 mJy, respectively. Also cross-correlated with NVSS source 175252–293000 with flux density of 4.1 mJy. The confusion with a nearby, radio brighter (~ 40 mJy at 1.4 GHz) NVSS radio source 175256–293044 is possible.

(15) G302.3–00.5 (PHR1246–6324; Fig. A3): Small bipolar PN, clearly visible in the radio. The radio source is centred on the PN and shows possible extended structure in a direction opposite to possible bipolar outflows. It is not clear if this structure is related to the PN or is it a faint background source.

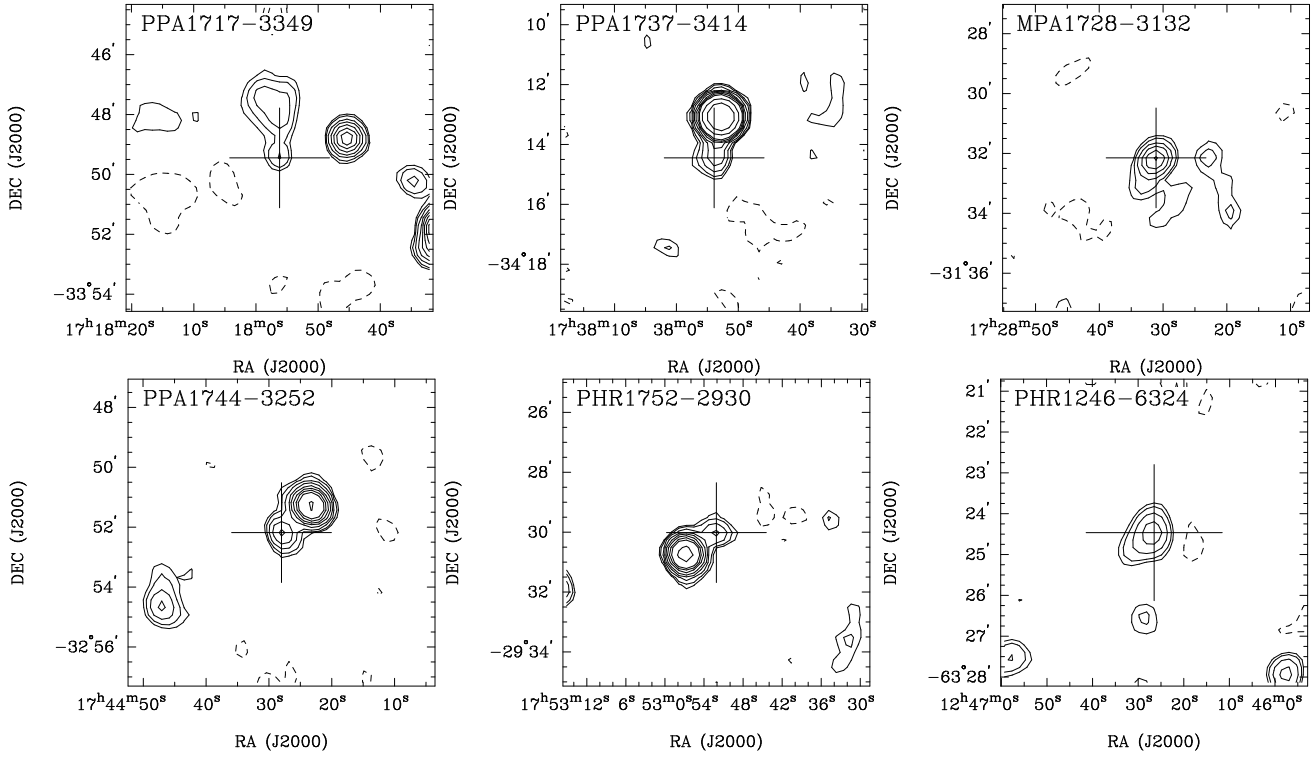


Figure A3. Same as in Fig. A2. First row (from left to right): PPA1717–3349 (NVSS), PPA1737–3414 (NVSS) and MPA1728–3132 (NVSS). Second row (from left to right): PPA1744–3252 (NVSS), PHR1752–2930 (NVSS) and PHR1246–6324 (MGPS-2).

(16) G291.6–00.2 (PHR1115–6059; Fig. A4): Bright, large (~ 100 arcsec), circular nebula designated as “likely” PN. Radio detection at 0.843 GHz appears to be associated with the $H\alpha$ bright NW edge. Estimated flux density is flagged as the low limit due to the marginal detection.

(17) G337.4+02.6 (PHR1625–4522; Fig. A4): Very large, diffuse nebula designated as a “likely” PN in MASH. The radio counterpart (not catalogued in the MGPS-2) is a faint “patch” of extended emission placed over the brighter nebular region. Estimated flux density is flagged as the low limit.

(18) G356.6–01.9 (PHR1745–3246; Fig. A4): Confirmed, slightly extended PN with central concentration with a radio counterpart catalogued in the MGPS-2. From Fig. A4 can be seen that radio peak is slightly offset from the brightest part of nebulosity. Apparent extension in the SN direction is an effect of the beam elongation due to the low declination.

(19) G013.3+01.1 (PHR1810–1647; Fig. A4): Slightly oval, confirmed PN, with prominent internal structure. The NVSS detection peaks over the brightest part of the possible shell. Estimated flux density is flagged as the low limit due to the marginal detection.

(20) G222.5+07.6 (BMP0736–0500; Fig. A5): Relatively large (~ 80 arcsec), extremely faint elliptical PN. The suspect radio detection from the NVSS is placed on the brighter part of the nebula.

(21) G247.5–04.7 (PHR0742–3247; Fig. A5): Large, elliptical, diffuse PN. The NVSS detection is suspected (barely above $1\sigma_{rms}$ local noise level) and coincides with the brightest parts of the shell.

(22) G254.5–02.7 (PHR0808–3745; Fig. A5): Large, diffuse nebula designated as “likely” PN. The NVSS suspect radio detection is placed on the brighter part of the nebula.

(23) G297.0–04.9 (PHR1150–6704; Fig. A5): S-bar shaped, confirmed PN, with internal knots. Radio detection (MGPS-2) is suspect due to the relatively large offset from the $H\alpha$ bright region. However, it is important to emphasise the similarity with position and extent of radio-peak offset seen in PHR1739–3829.

(24) G309.5+00.8 (PHR1346–6116; Fig. A5): Partial arcuate nebula with sharp western edge, designated as “likely” PN. A faint radio source found in MGPS-2 (not catalogued) is placed over the fainter region and it is considered as suspect.

(25) G324.3+01.1 (PHR1529–5458; Fig. A5): Possible PN, with strongly elongated, irregular emission and with possible superposed arcuate nebula. The associated radio source from MGPS-2 is extended and approximately follows the brightness distribution of $H\alpha$ emission. However, as can be seen from the presented histogram equalised quotient image, the radio peak is placed over the low $H\alpha$ emission region. The nebula is approximately twice the size of the MOST synthesised beam FWHM.

(26) G332.3+07.0 (PHR1547–4533; Fig. A5): Very faint, circular nebula designated as a “likely” PN in MASH. The radio detection at 0.843 GHz appears extended but covers only the inner (fainter) part of the nebula.

(27) G351.1–03.9 (PHR1739–3829; Figure A5): Bright, bipolar, confirmed PN. As in the case of PHR1748–3538, the radio emission at 1.4 GHz appear to be generally correlated with the $H\alpha$ but with a radio peak ~ 20 arcsec from the brightest

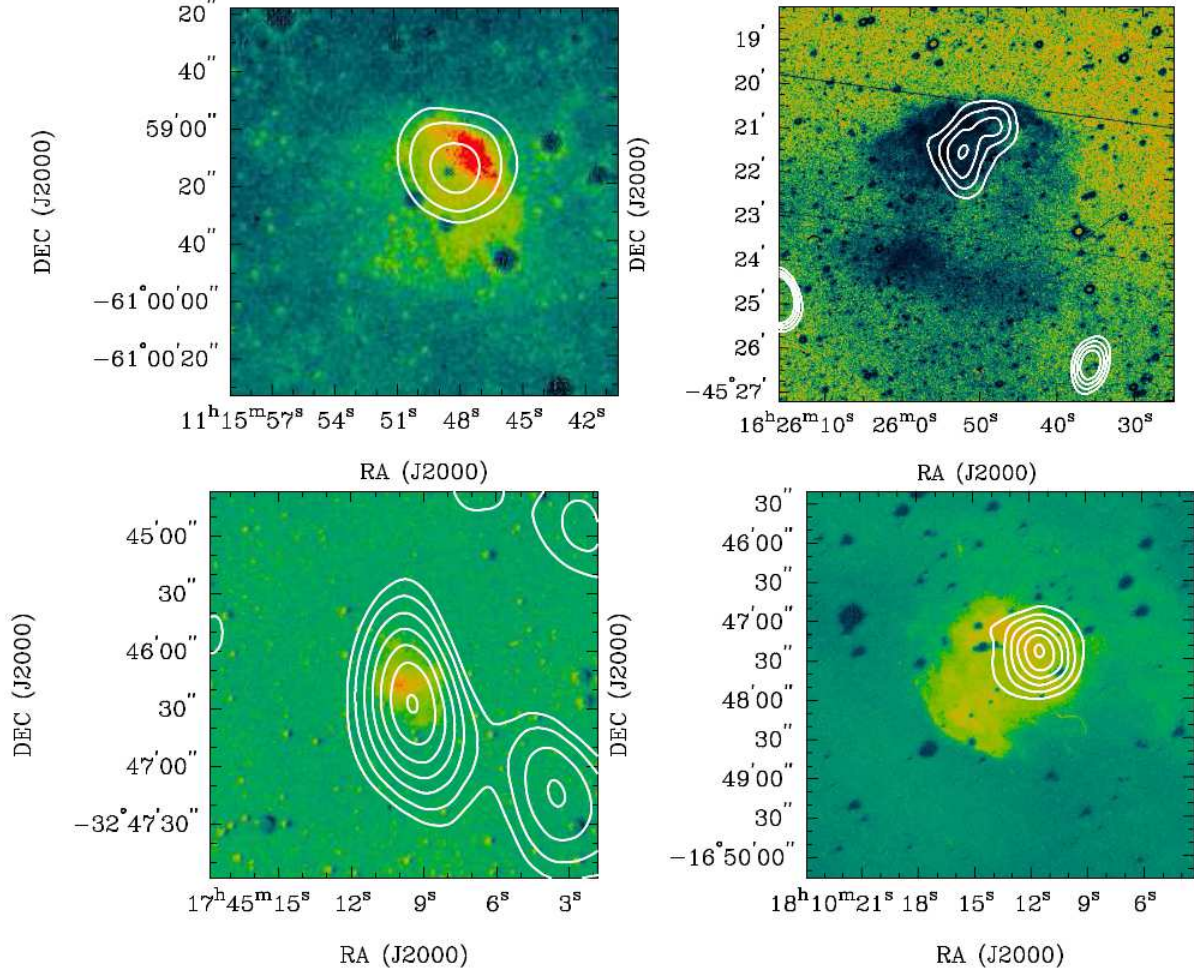


Figure A4. Finding charts of MASH PNe with MGPS-2/NVSS radio counterparts. Finding charts are produced as radio-continuum contour maps from the MGPS-2/NVSS superposed on the SHS *quotient* images (see text for more details). **Top left:** PHR1115-6059, the MGPS2 radio contours are at 6, 10 and 15 mJy; **Top right:** PHR1625-4522, the MGPS2 radio contours are at 6, 8, 10 and 12 mJy; **Bottom left:** PHR1745-3246, the MGPS2 radio contours are at 6, 10, 15, 20, 25, 30, 35 mJy; **Bottom right:** PHR1810-1647, the NVSS radio contours are at 1.5, 2, 2.5, 3, 3.5, and 4 mJy; Images for PHR1115-6059, PHR1745-3246 and PHR1810-1647 were produced as log scaled SHS *quotient* images and for PHR1625-4522, as histogram equalized SHS *quotient* image.

parts of the nebula. In contrast to of the PHR1748–3538, the radio “wings” are, in this case, in the direction of possible bipolar outflows. It is flagged as a suspect radio detection.

(28) G354.5–03.9 (PHR1748–3538; Fig. A5): Oval ring PN with faint outer extensions, designated as a true PN with optical dimensions 56×39 arcsec. As stated in LCY05, the bright radio peak is about 60 arcsec away from the optical centroid. A bright offset radio source is catalogued in NVSS as a possible complex object 174818-35375 with a flux density estimate of $S_{1.4\text{GHz}} = 44.4 \pm 1.8$ mJy. The flux density of the nebula itself is estimated to be $S_{1.4\text{GHz}} = 3.2 \pm 0.6$ mJy. Fig. A5 (left hand side panel in the bottom row) shows the histogram equalised quotient image overlaid with contours from the 1.4 GHz NVSS image. A bright, ring like structure is visible, with possible bipolar outflows. While the radio emission is extended in the direction of the bright region of nebulosity, the radio peak does not appear to be correlated with $\text{H}\alpha$ emission. We also found a nearby bright radio source in cross-correlation with the MGPS-2 catalogue. It peaks at a similar position to the NVSS bright source with a flux density at 0.843 GHz of 70.8 ± 2.6 mJy. The spectral index ($\alpha \approx -0.8$) of this object clearly points out to the non-thermal origin. Thus, we can definitely conclude non-association with the PN. Unfortunately, the mosaic containing this region (J1742M36) was not available and we have not been able to examine if similar extended emission, seen at 1.4 GHz, exists at 0.843 GHz. A faint radio source, to the left of the nebulosity, also does not appear to be associated with this PN.

(29) G015.5+02.8 (BMP1808–1406; Fig. A5): Very large (~ 470 arcsec), confirmed elliptical PN with enhanced opposing edges. The detection of the NVSS source placed over the bright SW $\text{H}\alpha$ emission region is flagged as a suspect and, regarding very low surface brightness of this PN, it is very likely that it is due to chance coincidence.

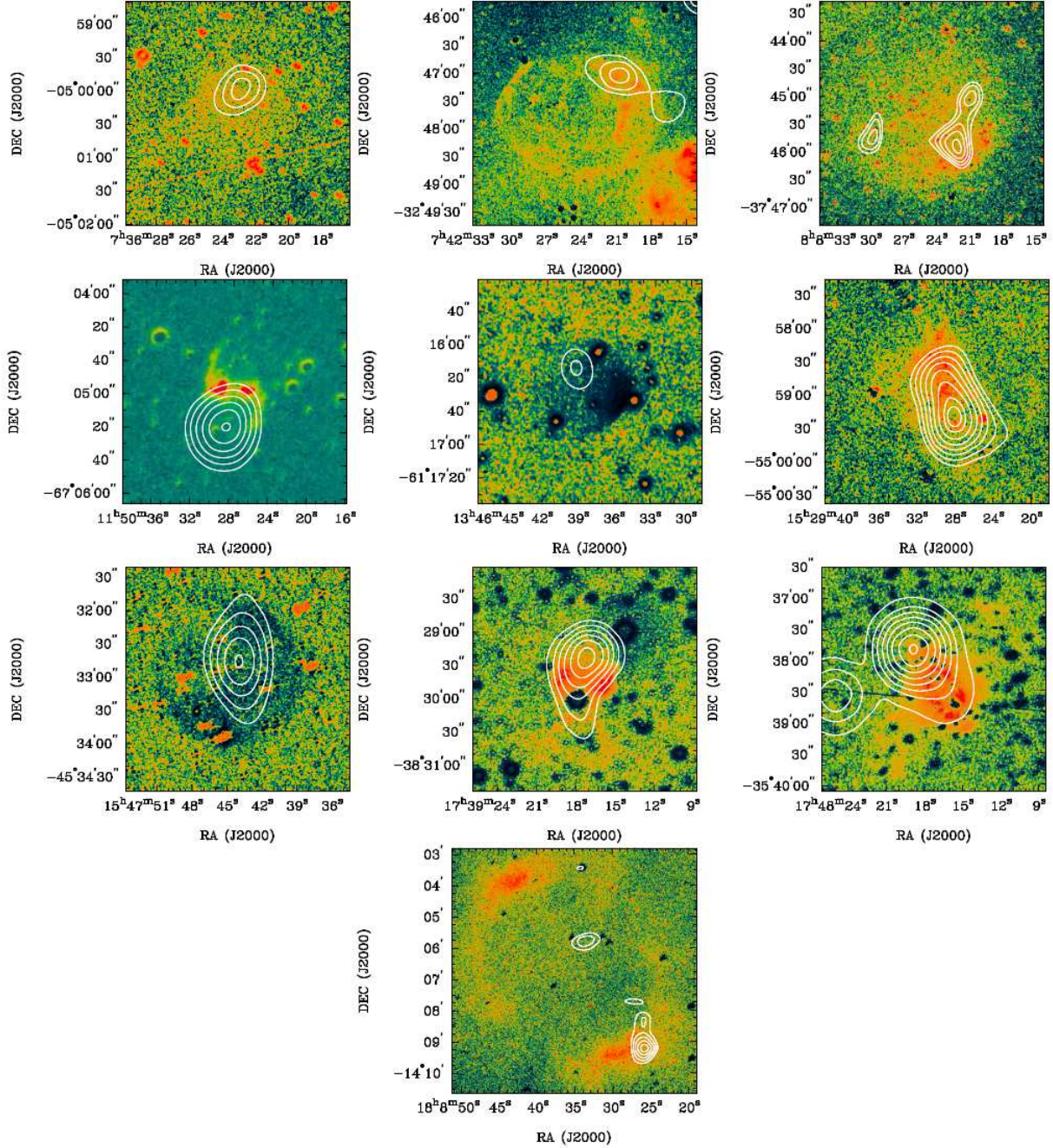


Figure A5. Finding charts of MASH PNe with MGPS-2/NVSS suspected radio counterparts. Finding charts are produced as radio-continuum contour maps from the MGPS-2/NVSS superposed on the SHS *quotient* images (see text for more details). **First row from left to right:** BMP0736-0500, the NVSS radio contours are at 1.5, 2 and 2.5 mJy; PHR0742-3247, the NVSS radio contours are at 1.5, 1.8, 2.1 mJy; PHR0808-3745, the NVSS radio contours are at 1.5, 1.6, 1.7, 1.8, 1.9 mJy; **Second row from left to right:** PHR1150-6704, the MGPS2 radio contours are at 6, 7, 8, 9, 10 and 11 mJy. PHR1346-6116, the MGPS2 radio contours are at 5 and 6 mJy. PHR1529-5458, the MGPS2 radio contours are at 6, 7, 8, 9, 10, 11, 12 and 12.5 mJy **Third row from left to right:** PHR1547-4533, the MGPS2 radio contours are at 6, 10, 15, 20 and 25 mJy; PHR1739-3829, the NVSS radio contours are at 2, 2.5, 3, 3.5, 4, 4.5 and 5 mJy; PHR1748-3538, the NVSS radio contours are at 2, 5, 8, 12, 17, 23, 30 and 38 mJy; **Fourth row:** BMP1808-1406, the NVSS radio contours are at 1.5, 2, 2.5, 3, 3.5, and 4 mJy; Images were produced as histogram equalized SHS *quotient* images except for PHR1150-6704 which is produced as log scaled SHS *quotient* image.

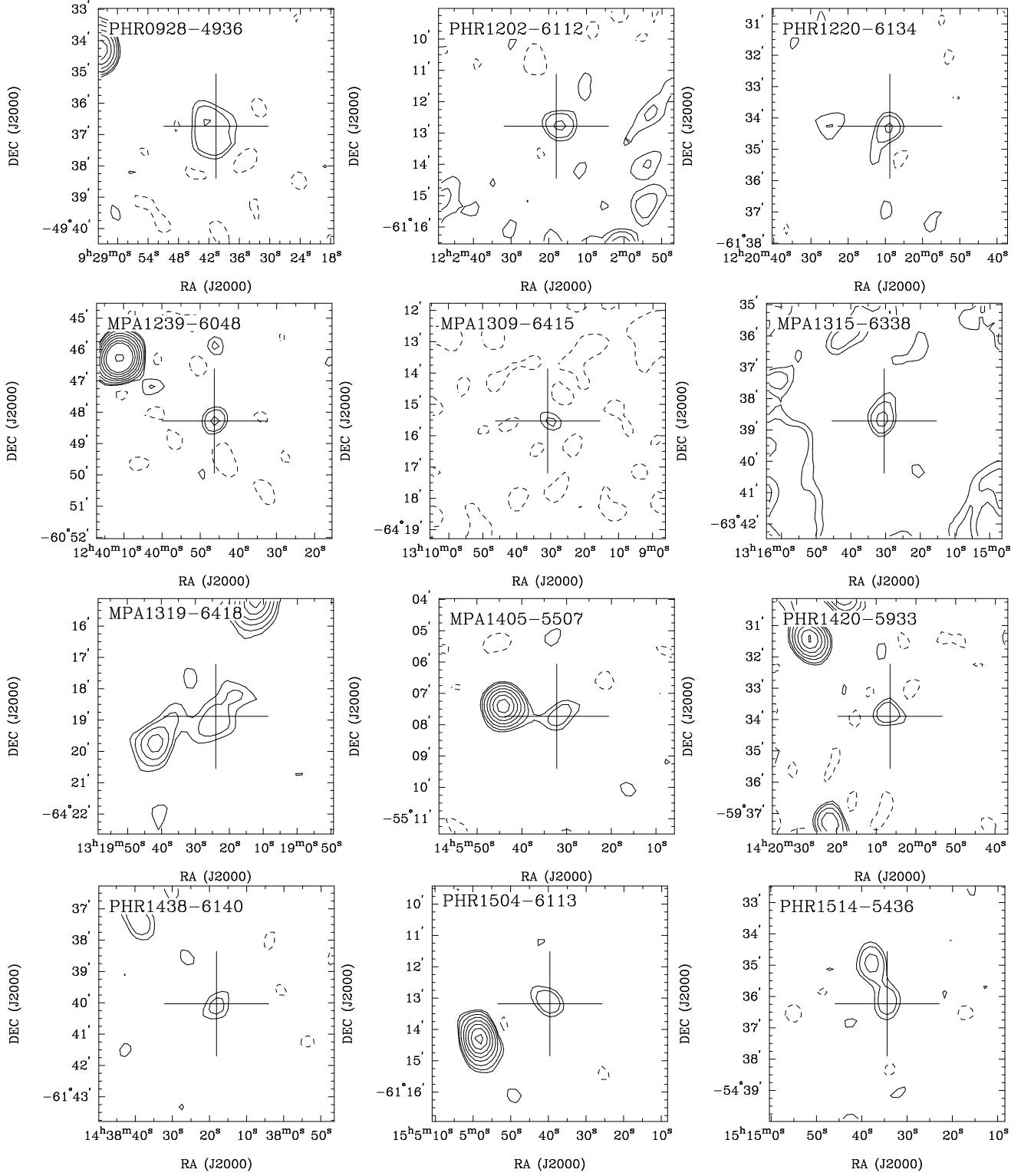


Figure A6. Radio-continuum contour plots of possibly radio detected MASH PNe in the MGPS-2 survey. None of these objects is catalogued in the MGPS-2 catalogue. Contours are at $-2, 2, 3, 5, 8, 12, 17, 23, 30, 60$ and $120 \times \sigma_{rms}$ (where σ_{rms} is a local rms noise). Negative contour (at $-2 \times \sigma_{rms}$) is presented with a dashed line. Radio-continuum contour images are overlaid with a cross centred in the MASH PN optical position. MASH PN designation is in the upper left corner.

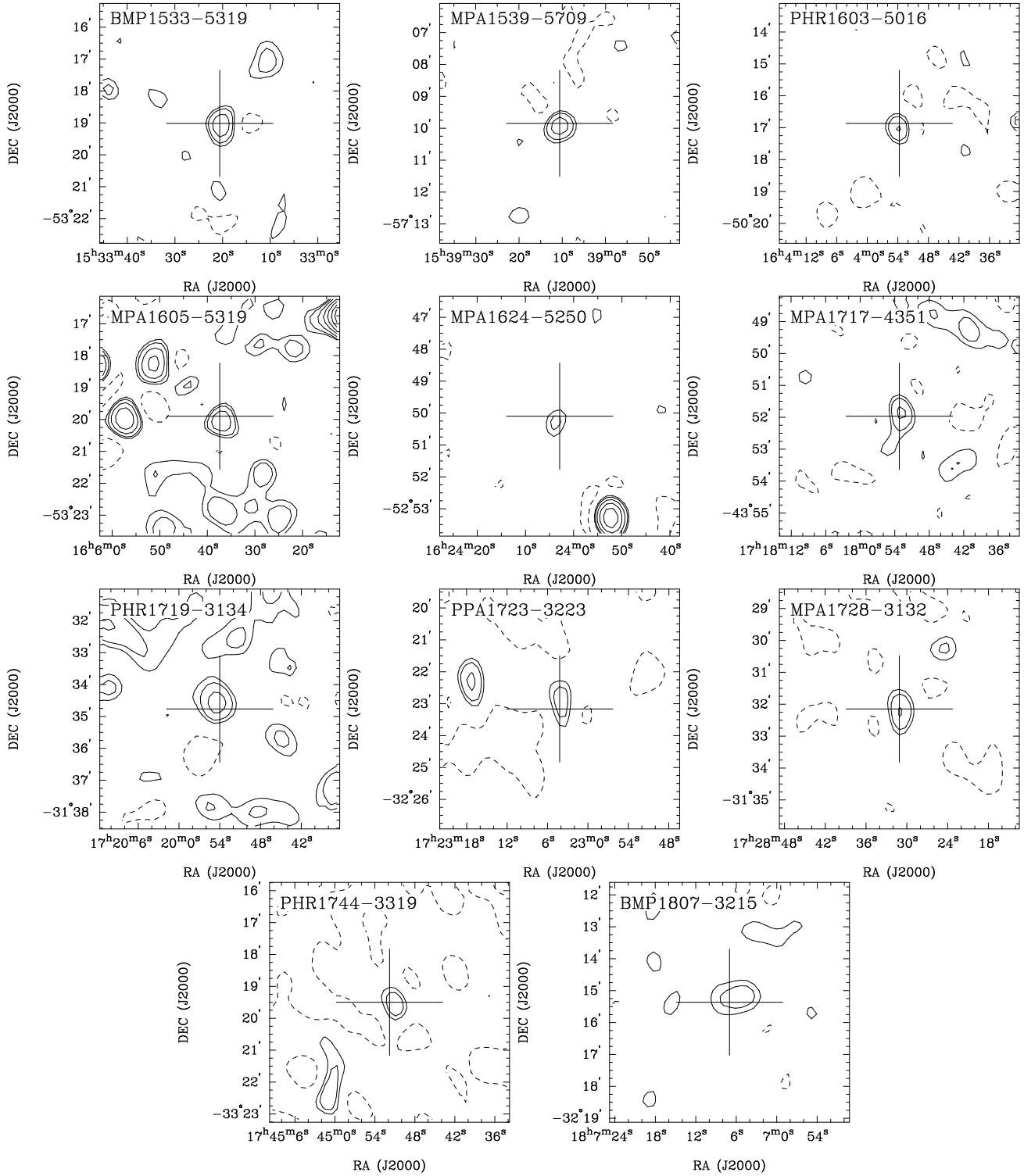


Figure A7. Same as in Fig. A6

APPENDIX B: MASH PNE WITH STEEP NEGATIVE RADIO SPECTRA

Several, apparently “True” MASH PNe, show a steep negative radio-continuum spectra. The negative spectral index implies nonthermal or strongly variable radio-continuum emission, both uncommon for PNe. We examined this set of objects in more detail.

PPA1722–3317 (PNG353.6+01.7; $\alpha_{0.843/1.4}^* = -0.5 \pm 0.3$) is a compact (4 arcsec) true PN. It is detected in NVSS with flux density $S_{1.4\text{GHz}} = 14.6 \pm 0.7$ mJy and it has a catalogued counterpart in MGPS-2 with a flux density $S_{0.843\text{GHz}} = 18.6 \pm 2.9$ mJy ($F_{0.843\text{GHz}} = 17.9 \pm 2.7$ mJy Beam⁻¹). The peak position of the NVSS source is within 1 arcsec from its optical counterpart. However, the MGPS-2 detection appears to be offset with distance from the optical centroid by more than 10 arcsec. The radio object has a high brightness temperature of more than 10^3 K at frequencies below 1 GHz. Thus, if this object is a true PN, as seems likely, then, according to its high brightness temperature, it is very likely a young and compact nebula. Thus, we would expect to see a rapid rise in flux densities toward higher frequencies. In order to resolve this discrepancy this object is scheduled to be observed at 3 cm and 6 cm (Bojičić et al. in prep.).

PPA1725–3216 (PNG354.8+01.8; $\alpha_{0.843/1.4}^* = -1.1 \pm 0.4$) is a confirmed, compact ($\theta_{\text{opt}} \approx 8 \times 6$ arcsec) PN with strong emission lines. Radio-continuum detections at 1.4 GHz ($S_{1.4\text{GHz}} = 10.0 \pm 0.6$ mJy) and 0.843 GHz ($S_{0.843\text{GHz}} = 17.6 \pm 3.4$ mJy) are well aligned with the optical position with small angular offsets of ~ 2.5 arcsec and ~ 3.5 arcsec. The steep negative radio spectra points to non-thermal emission as the main emission mechanism at cm wavelengths. Additional observations are needed to resolve the true nature of this object.

PPA1729–3152 (PNG355.6+01.4; $\alpha_{0.843/1.4}^* = -0.7 \pm 0.4$) is a compact (6×5 arcsec), probable very low excitation (VLE) PN with very strong lines in the red including [ArIII]. This object is designated only as “likely” PN. The radio counterpart seen at 1.4 GHz ($S_{1.4\text{GHz}} = 8.2 \pm 0.6$ mJy) and at 0.843 GHz ($S_{0.843\text{GHz}} = 11.6 \pm 2.1$ mJy and peak flux $F_{0.843\text{GHz}} = 11.2 \pm 2.1$ mJy Beam⁻¹) is within 3 arcsec radius from the optical centroid. The MGPS-2 detection is close to the catalogue detection threshold and, additionally, the object appears to be placed in a noisy region. In order to resolve the true nature of the radio-continuum emission mechanism from this object additional observations are needed.

PHR1753–3443 (PNG355.9–04.4; $\alpha_{0.843/1.4}^* = -0.6 \pm 0.2$) is a confirmed, bipolar PN with newly identified WR spectral features from the central star (DePew et al. 2010) and an angular size of 27×15 arcsec. The found flux densities are $S_{1.4\text{GHz}} = 15.0 \pm 0.7$ mJy and $S_{0.843\text{GHz}} = 20.9 \pm 1.8$ mJy. Both NVSS and MPGS-2 peak positions are slightly offset from the optical centroid (~ 6 arcsec and ~ 7 arcsec, respectively) but still well within the visible nebulosity. Even though a possibility of chance coincidence detection exists it is very likely that the radio-continuum detections are genuine. A small offset indicates the possibility that the detected radio-continuum emission is coming from a region much smaller than the visible nebular extent.

PHR1755–2904 (PNG001.0–01.9; $\alpha_{0.843/1.4}^* = -2.3 \pm 0.4$) is a compact, bright, slightly oval true PN with faint outer halo and angular diameter of 14.5×12.5 arcsec. It is detected in NVSS with measured flux density $S_{1.4\text{GHz}} = 4.8 \pm 0.6$ mJy and it has a catalogued counterpart in MGPS-2 with a flux density $S_{0.843\text{GHz}} = 15.5 \pm 2.3$ mJy. Radio peak offsets, for both radio-continuum detections, are smaller than 3 arcsec. Unfortunately, the SUMSS/MGPS-2 mosaic cut-out is not available from the postage stamp server so we could not examine the possibility of some confusing source at 0.843 GHz. In order to resolve this discrepancy this object was observed at 3 cm and 6 cm (Bojičić et al. in prep.).

PHR1758–1841 (PNG010.2+02.7; $\alpha_{1.4/5}^* = -0.9 \pm 0.2$) is a spectroscopically confirmed, compact, circular PN with angular diameter of 8 arcsec. The NVSS detection, with flux density $S_{1.4\text{GHz}} = 18.3 \pm 0.7$ mJy, and detection at 5 GHz, with flux density $S_{5\text{GHz}} = 6.1 \pm 1.5$ mJy (Ratag & Pottasch 1991) are placed over the central part of this nebula with offsets between the radio peak and optical centroid of 1 and 3 seconds of arc, respectively. The WSRT observation (5 GHz) was performed with the synthesised beam FWHM of about 3–6 arcsec in α and 15–35 arcsec in δ (Ratag & Pottasch 1991). Thus, due to the small angular diameter of this PN, we believe that the large negative spectral index cannot be accounted to the missing flux problem. In order to resolve the true nature of this object additional observations are needed.